Research Square

Preprints are preliminary reports that have not undergone peer review.
They should not be considered conclusive, used to inform clinical practice,
or referenced by the media as validated information.

Conceptual design and first-order performance assessment of a tri-source hybrid (solar–hydrogen–battery) long-endurance UAV for extreme climates

Ümit Deniz Göker

udenizg@gmail.com

Epistemic Research Frameworks (ERF), Independent Research Institute

Research Article

Keywords: Conceptual aircraft design, Extreme-climate operation, Hybrid-electric UAV, Inertial particle separator, PEM fuel cell, Solar–hydrogen propulsion

Posted Date: November 19th, 2026

DOI: https://doi.org/10.21203/rs.3.rs-11680163/v1

License: This work is licensed under a Creative Commons Attribution 4.0 International License.
Read Full License

Additional Declarations: Competing interest reported. The author is the inventor named in European patent application EP 26211841.7, “Tri-source hybrid long-endurance unmanned aerial vehicle” [13], which covers the configuration described in this paper.

Conceptual design and first-order performance assessment of a tri-source hybrid (solar–hydrogen–battery) long-endurance UAV for extreme climates

Ümit Deniz Göker[1]

Abstract

Small long-endurance unmanned aerial vehicles (UAVs) for hot-desert and polar operation face conflicting requirements: solar power is intermittent, hydrogen fuel cells need clean, temperature-conditioned air, and dust, sand, rain, and icing threaten every air-breathing subsystem. This paper presents the conceptual design of Eastern Hornet, a 60 kg tri-source hybrid UAV that combines a photovoltaic array covering 85% of the wing area, an air-cooled proton-exchange-membrane fuel cell, and a lithium-ion buffer battery on a common DC bus. The fuel cell is fed by a ram-air intake on the lower wing surface near the root, which does not shade the solar array and contains a passive inertial particle separator with electrothermal anti-icing. A common battery-powered heating subsystem supports fuel-cell cold start and sensor thermal management over a design operating range of −50 °C to +50 °C. First-order sizing gives a wing area of 7.5 m², an aspect ratio of 14 and a span of 10.25 m. A low-fidelity aerodynamic assessment gives a zero-lift drag coefficient of 0.021–0.028, cruise and loiter electrical power of 1.70–2.27 kW and 0.77–0.98 kW, and hydrogen-only endurance of 5.3–7.1 h and 12.2–15.6 h, bracketing the design estimates. Two-dimensional RANS simulations confirm the section lift data and give exit flow angles of 23–46° and loss coefficients of 0.03–0.07 for separator vane angles of 30–60°; a three-dimensional RANS simulation gives a lift-curve slope of 5.6 per radian, a loiter angle of attack of about 2.0° and, with the baseline internal arrangement, a static margin of about 14%.

Keywords: Conceptual aircraft design · Extreme-climate operation · Hybrid-electric UAV · Inertial particle separator · PEM fuel cell · Solar–hydrogen propulsion

Nomenclature

AR	Wing aspect ratio, b^2/S
b	Wing span (m)
$\bar{c}$	Mean geometric chord, S/b (m)
C_D, C_{D0}, C_{Di}	Drag, zero-lift drag and induced-drag coefficients
C_L, C_{Lmax}	Lift and maximum lift coefficients
c_p	Specific heat of air at constant pressure (J kg^{-1} K^{-1})
D	Drag (N)
e	Oswald span efficiency factor
L	Fuselage length (m)
l_h, l_v	Horizontal and vertical tail arms (m)
$\dot{m}_{cool}$	Mass flow of cooling air (kg s^{-1})
P_{el}	Electrical power required (W)
$P_{el,\,FC}$	Electrical power of the fuel cell (W)
Re	Reynolds number based on $\bar{c}$
S	Wing reference area (m²)
S_h, S_v	Horizontal and vertical tail areas (m²)
V, V_s	Airspeed and stall speed (m s^{-1})
V_H, V_V	Horizontal and vertical tail volume coefficients

[1] Independent Researcher, Epistemic Research Frameworks (ERF), Independent Research Institute, Québec, Canada

✉ Ümit Deniz Göker: udenizg@gmail.com

W	Weight at maximum take-off mass (N)
ΔT	Allowed cooling-air temperature rise (K)
η	Combined motor and propeller efficiency
λ	Cathode air stoichiometric ratio
ρ	Air density (kg m^{-3})

1. Introduction

1.1. Motivation

Small and medium unmanned aerial vehicles (UAVs) are increasingly expected to fly long missions in environments that are hostile to both aircraft and crews: hot deserts with airborne sand and dust, polar regions with very low temperatures and long periods of darkness, and humid tropical regions with persistent rain. Search and rescue, environmental and glaciological survey, and the monitoring of borders and remote infrastructure all benefit from endurance measured in tens of hours and from the ability to operate from short, unprepared strips far from maintenance facilities.

Solar-electric propulsion has become the reference technology for endurance, and its status has recently been reviewed in detail [1]. At stratospheric altitude, the Airbus Zephyr remained aloft for about 64 days in 2022 before the flight ended in a crash [2], and the 35 m span PHASA-35 climbed above 66,000 ft in its first stratospheric trial in 2023 [3]. At small scale, the 6.9 kg AtlantikSolar flew continuously for 81 hours and 2,338 km [4]. These results, however, rely on very low wing loading, very high aspect ratio, and favourable seasons and latitudes. Solar input disappears at night and is strongly reduced at high latitudes, in winter, and under cloud, which are precisely the conditions of many polar and all-weather missions, and storing a whole night of energy in batteries scales poorly with mass.

Hydrogen fuel cells offer a much higher stored energy per unit mass than batteries. The U.S. Naval Research Laboratory's Ion Tiger flew for 26 h 2 min in 2009 on compressed hydrogen and for 48 h 1 min in 2013 on liquid hydrogen [5]. Reviews of hybrid UAV power systems conclude that combining fuel cells, batteries, supercapacitors, and photovoltaic (PV) modules improves energy management, because each source can operate within its own limits [6], and rule-based energy management has been demonstrated for solar–battery mini UAVs [7]. Fuel cells, however, bring their own environmental vulnerabilities. A proton exchange membrane (PEM) stack needs a continuous supply of clean oxidant air, and freezing of product water makes start-up below 0 °C a well-known challenge [8]. Airborne sand and dust are a hazard for every air-breathing system; for helicopter engines operating from unprepared sites, this has led to vortex-tube separators, inertial particle separators, and inlet barrier filters [9, 10].

1.2. Related work and research gap

In all of the solar-electric aircraft cited above, the PV cells are mounted on the upper wing surface, and none of them needs an air intake, because no part of the power system breathes air. The closest published concept is the solar–hydrogen–battery "tribrid" UAV announced in 2025 by H3 Dynamics and XSun, built on the SolarXOne platform, in which batteries are used for take-off, a hydrogen fuel cell for cruise, and solar energy to extend flight time; prototype test flights were planned for October 2025 [11]. Its architectural details, in particular the location and protection of the fuel-cell air intake, are not public. Work on integrating composite hydrogen pressure vessels into small aircraft is also progressing [12].

A public-domain search of the literature and of patent databases, carried out for the European patent application on which this paper is based [13], did not identify a published

design that combines (i) a PV array on the upper wing surface, (ii) a ram-air intake on the lower wing surface near the root that supplies both oxidant and cooling air to an air-cooled PEM fuel cell, and (iii) a passive particle separator with no moving parts and electrothermal anti-icing inside that intake, for an operating envelope of approximately −50 °C to +50 °C. This search was limited to publicly accessible sources and is not a formal patentability search.

1.3. Contributions and structure of the paper

The contributions of this paper are as follows:

- An all-electric tri-source architecture (PV array, air-cooled PEM fuel cell and lithium-ion buffer battery on a common DC bus) in which the PV array occupies the upper wing surface and the fuel-cell air intake occupies the lower wing surface near the root, so that the intake does not shade the array.
- A multi-climate intake that performs both oxidant supply and convective cooling through a single passive inertial-separator geometry with no moving parts and no replaceable filter, complemented by electrothermal anti-icing, together with a first-order airflow budget that separates the oxidant and cooling requirements.
- A common battery-powered heating subsystem for fuel-cell cold start, sensor-bay and flight-computer thermal management, with its energy cost included in the endurance budget.
- A first-order sizing of the aircraft (MTOW 60 kg, S = 7.5 m², AR = 14), including a clear-sky estimate of the daily solar energy yield in a hot-desert and a high-Arctic location, a baseline internal arrangement with a centre-of-gravity and static-margin estimate, and an independent low-fidelity aerodynamic assessment with open-source tools which shows that the design estimates fall within the computed ranges.
- Two-dimensional RANS simulations of the wing section and of the separator vane row, which quantify the effect of boundary-layer transition on the profile drag and the turning, loss and pressure drop of the separator.
- A three-dimensional RANS simulation of the complete aircraft in the clean configuration on three successively refined meshes, which confirms the lift and the trim condition of the sizing and quantifies the numerical uncertainty of the computed lift and drag.
- A test plan for the experimental validation of the complete aircraft, the wing section and the separator vane row.

Section 2 describes the configuration and system architecture. Section 3 presents the sizing methodology, including the internal arrangement and centre of gravity, the solar energy yield and the hydrogen energy budget. Section 4 reports the aerodynamic assessment and compares it with the design estimates, and Section 5 outlines the planned experimental validation. Section 6 discusses limitations and sensitivities, and Section 7 concludes the paper.

2. Configuration and system architecture

2.1. General layout

Eastern Hornet is a conventional fixed-wing aircraft with a single slender fuselage, a high-aspect-ratio wing, a conventional tail and an electrically driven pusher propeller (Fig. 1; Online Resource 1). Its main dimensions are given in the three-view drawing of Fig. 2. In this drawing, the values that follow from the sizing of Sect. 3 are distinguished from representative values chosen for the drawing. Numerals in parentheses refer to the components of the patent

application [13]. The three-dimensional model was generated parametrically with the Python interface of Blender 5.2 (Blender Foundation), and the dimensioned drawing was produced from the same geometry definition with Matplotlib.

The fuselage, about 4.2 m long, carries in its nose a stabilised gimbal turret with fused thermal and low-light sensors (1a). A nadir-looking mapping bay (1c) is located in the lower centre fuselage close to the centre of gravity, and the fuselage air-intake mouth (1b) is placed beside it, offset so that neither the airflow into the intake nor the field of view of the mapping bay is obstructed.

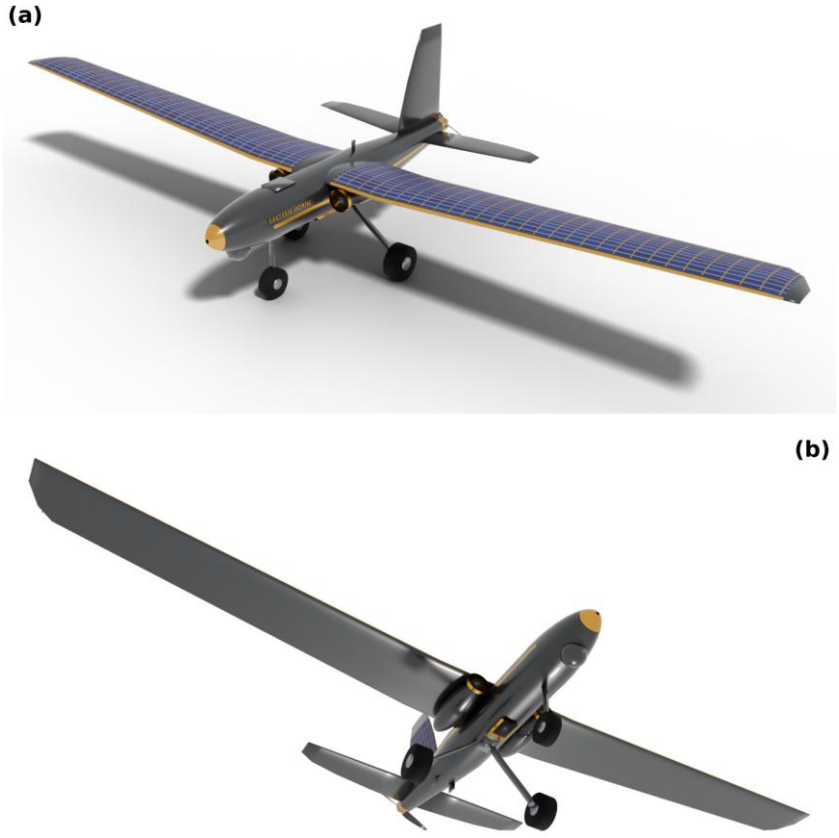


Figure 1. Three-dimensional model of Eastern Hornet: **(a)** upper three-quarter view showing the photovoltaic array on the upper wing and fin surfaces; **(b)** underside view showing the air intakes on the lower wing surface near the root, the fuselage intake and the landing gear. The geometry is that of Fig. 2 and of the aerodynamic analysis of Sect. 4; colours and surface finish are illustrative. An interactive version of the model is provided as Online Resource 1.

The wing has a slight dihedral break at the root: the inner panels run almost horizontally, while the outer panels carry the dihedral (4° in the present layout). The break gives structural room under the fuselage for the intake mouth and the landing gear.

The PV array covers the upper surface of the wing (2a), about 85% of the wing reference area. The air intakes (2b) are on the lower surface of the wing near the root, where they do not shade the array, and are connected to the fuel cell through internal ducts (2c). The tail is conventional, with a single fin and a horizontal stabiliser; part of the fin is covered by a secondary PV panel (3a) connected to the same DC bus. Fuselage, wing and tail are made from a carbon-fibre prepreg of the HexPly 8552/IM7 class, an amine-cured toughened epoxy developed for primary aerospace structures and for service temperatures up to 121 °C [14], well above the +50 °C hot end. Leading edges are protected against sand erosion and rain

impact by a thin polyurethane erosion tape of the type used on helicopter rotor blades [15], and the outer surface carries a UV-resistant polyurethane topcoat.

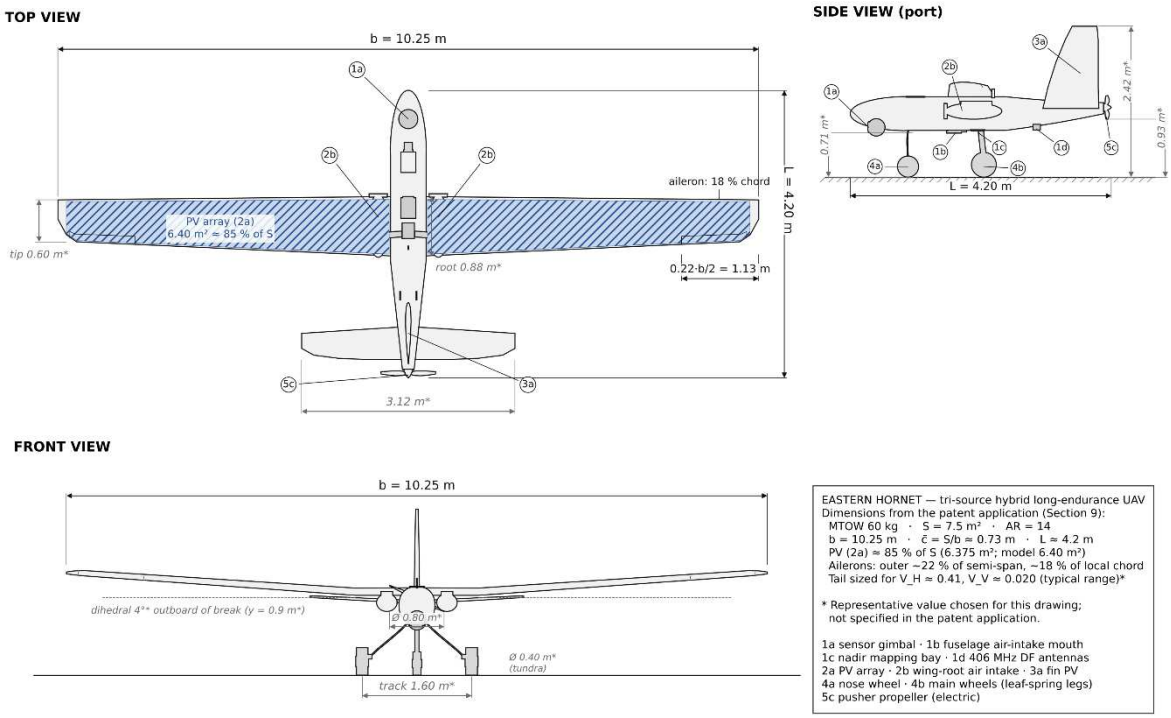


Figure 2. Dimensioned three-view (top, front and port side). Black: values from the sizing of Sect. 3 and the patent application [13]; grey and marked *: representative values chosen for this layout. Part numerals follow the patent figures.

2.2. Tri-source power architecture and power management

The aircraft is entirely electric: there is no combustion engine and no direct turbine thrust. Three sources feed a common DC bus (Fig. 3). The PV array is divided into many independent segments along the span, each with its own maximum power point tracking (MPPT) converter and bypass diodes, so that partial shading or varying sun angle on one part of the wing does not pull down the rest of the array. The fuel cell (5a) is connected to the bus through a unidirectional DC–DC converter with reverse-current blocking, which prevents current from flowing back into the stack when the bus voltage exceeds the stack voltage, a known cause of catalyst-layer damage. The lithium-ion battery (5b) is connected directly and bidirectionally to the bus; it buffers transients and supplies the fuel-cell pre-heating circuit (Sect. 2.4). PEM fuel-cell systems for UAVs in the relevant power class are commercially available; for example, the H3 Dynamics Aerocell series is listed with rated powers of 250–2,000 W [16], which corresponds to roughly 350–560 W/kg when the listed rated power is divided by the listed dry mass.

Figure 3 also shows the air and hydrogen circuits. Air from the two wing-root intakes (2b) passes the electrothermal anti-icing element (HE1) and the inertial separator, which discharges the separated particles overboard, and reaches the plenum of the stack through the ducts (2c) inside the wing; the fuselage intake mouth (1b) feeds the same plenum. The stack fan draws the air through the open cathode, which serves as both oxidant supply and cooling channel, and the warm, humid air leaves through the exhaust. Hydrogen flows from the 70 MPa vessel through an on-tank shut-off valve with a thermally activated pressure-relief device and a first-stage regulator, through a second shut-off valve and a second-stage regulator to the dead-ended anode, which is purged periodically into the cathode exhaust, where the

hydrogen is diluted. These are established balance-of-plant components: open-cathode fuel-cell systems for UAVs use a regulated hydrogen supply and a dead-ended anode with a periodically opened purge valve [17], solenoid shut-off valves and high-pressure regulators are available for 70 MPa storage [18], and thermally activated pressure-relief devices for compressed-hydrogen vehicle containers are specified in ISO 19882 [19].

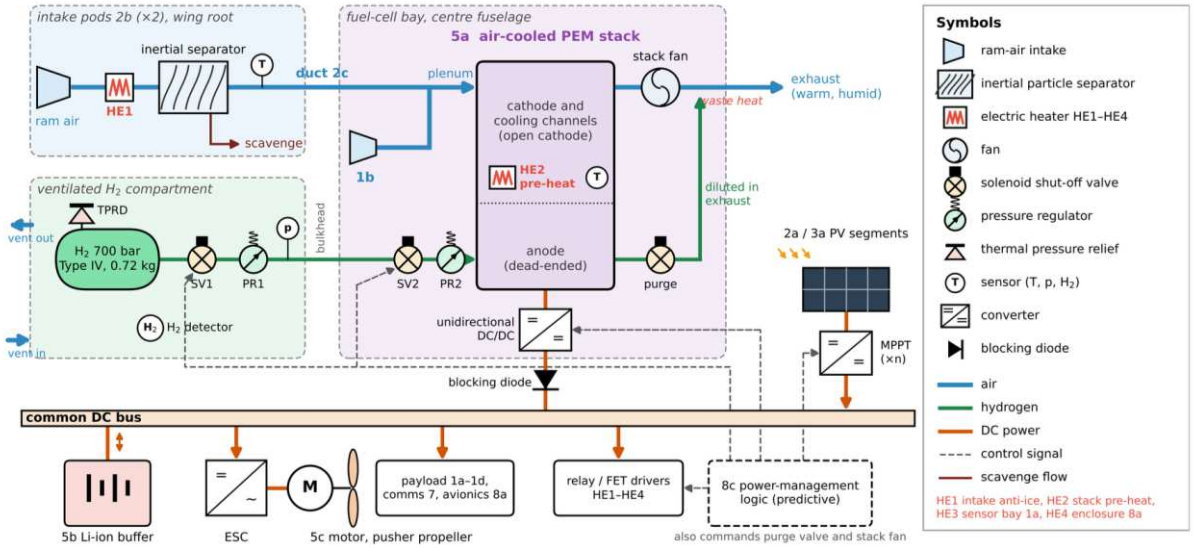


Figure 3. Air, hydrogen, heating and electrical circuits of the tri-source power system (baseline). The zones correspond to the internal arrangement of Sect. 3.4. HE1–HE4: electric heaters; SV1, SV2: solenoid shut-off valves; PR1, PR2: pressure regulators; TPRD: thermally activated pressure-relief device; *T*, *p*, H_2: temperature, pressure and hydrogen sensors; dashed lines: control signals of the power-management logic (8c).

The power-management logic (8c) gives priority to the PV array whenever irradiance is sufficient, uses the battery to cover peaks and lets the fuel cell provide the base load, preserving the hydrogen reserve. The battery state of charge (SoC) is divided into three bands (indicatively ≤30%, 30–70% and ≥70%); the fuel-cell contribution is increased in the low band and reduced in the high band. The distinctive element is a predictive trigger: because pre-heating a cold stack takes minutes rather than seconds, the logic starts pre-heating the fuel cell in advance when it predicts that irradiance will fall (sunset computed from GNSS time and position, the PV current used as an irradiance proxy, or increasing cloud cover) or when the SoC approaches a threshold (indicatively about 35%, with a look-ahead of about 10–15 min). The logic uses only on-board data and directly drives the DC–DC converter and contactors and the relay or FET drivers of the heaters. The MPPT converters track their own maximum power points independently of this logic. All numerical thresholds are indicative and will be tuned to the final battery capacity, stack thermal mass, and flight profile.

2.3. Multi-climate air intake

The fuel cell is an air-cooled PEM stack with an open cathode: the cathode side is exposed directly to the bulk air flow from the intake rather than to a closed flow channel. The same flow therefore supplies oxygen for the electrochemical reaction (primary function) and removes heat from the stack and the battery by convection (secondary function), without valves, split ducts, or moving parts. At the cold end, this flow must not freeze the stack; at the hot end (+50 °C), it must prevent the membrane from overheating and drying out.

Instead of a replaceable filter, the intake contains a passive inertial (swirl) separator (Fig. 4). Curved static vanes on the inner wall, set at a helix angle of about 30–60°, turn the incoming flow into a swirling flow; particles denser than air, such as sand, dust, and rain

droplets, are thrown to the outer wall and leave through a scavenge port whose area is about 5–15% of the duct cross-section. The scavenge flow is driven only by the ram pressure gradient in the duct. A convergent section, reducing the area to about 60–80% of the inlet area, increases the velocity and therefore the separation effectiveness. The principle is the one used in engine air particle separators of helicopters [9, 10]. The vane surfaces are protected by the same polyurethane erosion coating as the leading edges, with harder metallic or ceramic tips as an option if field tests show heavy wear. A thin electrothermal heating element at the intake lip and over the vane region keeps the flow above freezing before it reaches the vanes, so that snow and ice cannot block the inlet. A light mesh guard can be fitted for missions with extreme sand loads, but the basic system works without any guard or filter.

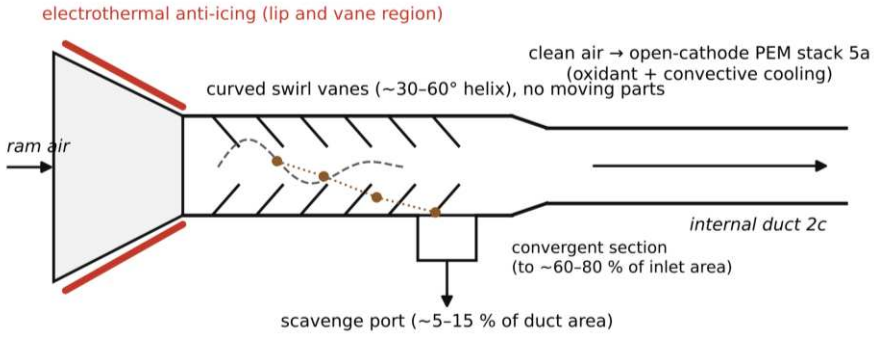


Figure 4. Schematic of the multi-climate intake with the passive inertial separator (not to scale).

Table 1 separates the two functions of the intake air. The oxidant requirement follows from Faraday's law for a cell voltage of 0.7 V. The cooling requirement assumes that the heat released by the stack is approximately equal to its electrical output, $P_{\mathrm{el,FC}}$ (stack efficiency about 50%) and that the cooling air may warm up by ΔT = 15–20 K. The required mass flow of cooling air, $\dot{m}_{\mathrm{cool}}$, then follows from the heat balance, with $c_{\mathrm{p}>}$, the specific heat of air at constant pressure:

$$\dot{m}_{\mathrm{cool}} = P_{\mathrm{el,FC}} / \left(c_{\mathrm{p}} \Delta T \right) \quad \textbf{(1)}$$

The volumetric flow of 120–350 L min^{-1} estimated in the patent application [13] corresponds to a stoichiometric ratio $\lambda \approx 2.4$–7.0 at the cruise power of 2.09 kW and therefore satisfies the oxidant requirement with a margin. Cooling, however, needs one to two orders of magnitude more air: about 2.8–3.7 m³ min^{-1} at loiter and 6.2–8.3 m³ min^{-1} at cruise. The intake flow budget is therefore set by cooling, not by oxidant. Even so, the required inlet area is small: with an inlet velocity ratio of 0.5, a total effective inlet area of about 0.005 m² at loiter and 0.008 m² at cruise is sufficient, i.e., two intakes with an effective diameter of about 6–7 cm each. The pressure loss of the separator must remain small compared with the available dynamic pressure, which is only 162 Pa at 18 m/s and 313 Pa at 25 m/s for ρ = 1.0 kg/m³.

Table 1. First-order air-flow requirements of the fuel cell (ρ = 1.0 kg/m³; oxidant flows at 0 °C and 1 atm)

Quantity	Loiter, 18 m/s (0.92 kW)	Cruise, 25 m/s (2.09 kW)
Oxidant air, λ = 1.5–2.0	33–44 L min^{-1}	75–99 L min^{-1}
Stoichiometry of 120–350 L min^{-1} [13]	$\lambda \approx$ 5.5–16	$\lambda \approx$ 2.4–7.0
Cooling air, ΔT = 20–15 K	2.8–3.7 m³ min^{-1} (0.046–0.061 kg s^{-1})	6.2–8.3 m³ min^{-1} (0.104–0.139 kg s^{-1})
Total effective inlet area (velocity ratio 0.5, ΔT = 20 K)	≈ 0.0051 m² (2 × Ø 5.7 cm)	≈ 0.0083 m² (2 × Ø 7.3 cm)
Dynamic pressure	162 Pa	313 Pa

Stack heat is assumed equal to electrical output; cell voltage is 0.7 V; c_p = 1005 J kg^{-1} K^{-1}. Pressure losses of the separator and spillage drag are not included.

2.4. Thermal management and fuel-cell cold start

The −50 °C end of the operating envelope is the most demanding point of the design. Freezing of product water inside the stack makes PEM start-up below 0 °C difficult and can damage the membrane electrode assembly [8]. The design therefore combines two measures: a controlled gas purge at shutdown, rather than complete drying of the membrane, and an electrical pre-heating circuit that raises the stack above freezing before start-up. The pre-heater is a simple resistive element supplied by the battery; it needs no combustion and no additional energy source, and its triggering is decided by the predictive power-management logic of Sect. 2.2.

The same battery-powered resistive approach is used throughout the aircraft as a common heating subsystem: it pre-heats and keeps warm the fuel-cell stack, heats the intake lip and vanes (Sect. 2.3), and keeps the sensor bay (1a) and the flight-control computer enclosure (8a) within the temperature ranges of commercially available components, which are typically narrower than −50 °C to +50 °C. The combined average heating power is estimated, to first order and indicatively, at 100–150 W; it is included as a separate item in the energy budget of Sect. 3.7 and will be refined by thermal analysis and field tests. At the hot end, the problem is reversed: the intake airflow that protects the stack from freezing in polar conditions protects it from overheating and membrane dry-out in the desert. The toughened epoxy resin of the structure was chosen for its impact and damage tolerance at low temperatures, which matters for hard landings and impacts in cold soak.

2.5. Landing gear and interchangeable ski module

The landing gear is a fixed tricycle with a nose wheel (4a) and two main wheels (4b). It has no retraction mechanism, so there are no actuators, hydraulic lines, or retraction linkages in which sand, ice, or mud could jam, consistent with the no-moving-parts philosophy of the intake. The wheels are wide, low-pressure “tundra” wheels that spread the load on loose sand or snow, and the main-gear track is wide (1.60 m in the present layout) to resist overturning on uneven ground and in strong crosswinds such as desert and katabatic winds. Each leg is a single composite leaf spring made from the same prepreg family as the airframe, so that the leg is both the structural member and the damper; this removes oleo-pneumatic struts and the risk of hydraulic-fluid viscosity problems at −50 °C. Composite leaf-spring legs are already in use on UAVs: UAVOS reports a leaf spring of aircraft-grade prepreg carbon fibre that is 38% stronger, thinner and lighter than its fibreglass equivalent (a manufacturer claim) [20]. Highly loaded metallic fittings such as axles and hubs are made from Ti-6Al-4V. The gear height keeps the pusher propeller and the fuselage intake mouth clear of spray from sand, mud or snow (Fig. 2).

For deep snow and ice, each leg end carries a common quick-connect interface, and the wheel unit (4b) can be replaced by a ski unit (4c). Unlike wheel-penetration skis, which are added over an existing wheel, the wheel and ski units are fully interchangeable modules; their masses and centre-of-gravity positions are matched as closely as possible, and the small remaining difference is closed with a calibrated ballast, so that mass, centre of gravity, and flight-control settings do not change.

2.6. Mission systems

The mission systems are summarised here; they are included in the mass budget but not analysed further in this paper. Comparable commercial products are cited to show that each function is available today and to document their rated operating temperatures (Table 2).

The nose turret (1a) combines thermal and low-light imaging in a single fused sensor core. Comparable units are the Teledyne FLIR Hadron 640R, which combines a 640 × 512 Boson thermal core with a 64 MP visible camera in a 56 g module [21], and the DJI Zenmuse H20N, a gimbal payload with dual 640 × 512 thermal cameras and a starlight camera [22]. Most UAV gimbals limit their pan travel to avoid cable wind-up; a slip-ring rotary joint, standard in surveillance pan–tilt cameras, allows unlimited 360° azimuth scanning.

The nadir bay (1c) accepts interchangeable modules through a standard mechanical and electrical interface: a LiDAR and RGB mapping unit such as the DJI Zenmuse L2 (905 g, detection range 450 m at 50% reflectivity) [23], a multispectral camera such as the MicaSense RedEdge-P (five multi-spectral bands, 350 g including the light sensor and cables) [24] or, for polar science, a ground-penetrating radar for snow and ice thickness and crevasse detection. An RTK/PPK GNSS receiver provides centimetre-level geolocation. The direction finder (1d) receives and decodes 406 MHz distress beacons (ELT, EPIRB and PLB) of the Cospas-Sarsat system, as the Becker Avionics BD406 emergency beacon locator does in manned aircraft [25]; the thermal camera then confirms the target.

Communications use three automatically switched layers: (i) a line-of-sight (LOS) RF data link; (ii) a low-Earth-orbit broadband satellite terminal, for which the Starlink Mini is representative (1.10 kg, 25–40 W average power, −30 °C to +50 °C, IP67) [26]; and (iii) a low-bandwidth link over the Iridium constellation, whose 66 active satellites in six near-polar planes (inclination 86.4°, altitude about 780 km) provide pole-to-pole coverage [27], as an always-on backup for telemetry, command and a compressed quick-look preview. Geostationary satellites were deliberately excluded because of their low elevation angle at high latitudes. All raw data are recorded on board and retransmitted when a high-bandwidth link becomes available, so that no data are lost.

The flight-control computer follows the architecture of commercial autopilots such as the CubePilot Cube Orange+, which has three redundant inertial measurement units, two barometers, and a redundant power supply with automatic failover [28]. It uses extended Kalman filter (EKF) state estimation and a lost-link protocol that returns the aircraft to its base or to a predefined landing site.

Table 2. Rated operating temperatures of comparable commercial components

Component	Function in Eastern Hornet	Rated operating temperature	Source
Teledyne FLIR Hadron 640R	Fused thermal/visible core (1a)	−20 to +60 °C	[21]
DJI Zenmuse H20N	Thermal/starlight gimbal (1a)	−20 to +50 °C	[22]
DJI Zenmuse L2	LiDAR + RGB mapping (1c)	−20 to +50 °C	[23]
MicaSense RedEdge-P	Multispectral option (1c)	0 to +40 °C (+50 °C with airflow)	[24]
Becker Avionics BD406	406 MHz beacon locator (1d)	−15 to +55 °C (short-term −40 to +70 °C)	[25]
Starlink Mini	LEO broadband terminal (7)	−30 to +50 °C	[26]

As Table 2 shows, none of these components covers the full −50 °C to +50 °C envelope, and the multispectral camera does not operate below 0 °C. The sensor bay, the payload modules and the flight computer are therefore placed in enclosures heated by the common heating subsystem of Sect. 2.4. The masses also show that the payload allowance of 1.61 kg in the mass budget of Sect. 3.2 (1a, the basic 1c module and 1d) is tight. The Zenmuse L2 alone weighs 905 g, and the BD406 direction finder weighs up to 700 g with its cockpit control head and up to 600 g, plus a mounting kit of up to 130 g, in its remote version without control head [25]. With the remote version, the three payload items add up to about 1.9–2.0 kg. The excess

of about 0.3–0.4 kg over the allowance is covered by the design and integration margin of 7.55 kg; it moves the centre of gravity aft by less than 1 cm and reduces the static margin of Sect. 3.4 from about 14% to about 13%.

3. Sizing methodology

3.1. Mission and design requirements

The design target is a medium-sized tactical UAV with a maximum take-off mass of 60 kg (Table 3). It is deliberately much smaller than stratospheric solar aircraft such as PHASA-35 (35 m span [3]), which are optimised for months-long flight at very low wing loading and have very limited manoeuvrability. Eastern Hornet is intended to fly at tactical altitude (1,500–3,000 m), to respond well to control inputs and to operate from short, rough strips. The sizing calculations use ρ = 1.0 kg/m³, which corresponds to an altitude of about 2,050 m in the International Standard Atmosphere (ISA), i.e., the middle of the operating band.

Table 3. Mission and design requirements

Requirement	Value
Maximum take-off mass (MTOW)	60 kg
Operating altitude	1,500–3,000 m (sizing at ρ = 1.0 kg/m³, ISA ≈ 2,050 m)
Cruise / loiter speed	25 m/s (90 km/h) / 18 m/s (65 km/h)
Ambient temperature range	approximately −50 °C to +50 °C
Operating environments	hot desert (sand, dust), polar (snow, ice, darkness), humid tropics (rain)
Field requirements	short, unprepared strips; no maintenance infrastructure
Roll-rate target	≈ 45–55 ° s^{-1} in the first-order sizing; 15–25 ° s^{-1} estimated for the present ailerons (Sect. 3.3)

3.2. Mass budget

The mass budget (Table 4) was set up with the statistical mass-fraction approach that is standard in conceptual aircraft design [29] and then cross-checked against component masses of comparable commercial products. Optional payloads (a multispectral camera of about 0.35 kg or a ground-penetrating radar of about 1.5 kg) are not part of the nominal budget; when fitted for a specific mission, they are taken from the design and integration margin of 12.6%.

Table 4. Mass budget at MTOW = 60 kg

Item	Mass (kg)	% MTOW	Section
Structure (fuselage, wing, tail; composite)	18.00	30.0	2.1
Fuel-cell stack + H_2 storage	12.00	20.0	2.2, 3.7
Battery pack	7.20	12.0	2.2
Propulsion (motor, propeller, ESC)	3.60	6.0	2.2
Wiring, distribution, actuators, other	3.00	5.0	—
PV array	2.55	4.25	3.6
Landing gear	2.40	4.0	2.5
Payload (1a + 1c basic + 1d)	1.61	2.68	2.6
Communication system	1.44	2.4	2.6
Flight control/avionics	0.65	1.08	2.6
Design and integration margin	7.55	12.6	—
Total (MTOW)	**60.00**	**100**	

3.3. Wing and tail sizing

A wing loading of $W/S \approx 8$ kg/m² was chosen as a compromise between a low stall speed, a large area for the PV array, and acceptable gust response; typical values for tactical UAVs lie between about 5 and 15 kg/m². This gives a wing area of $S = 60/8 = 7.5$ m². The aspect ratio was deliberately kept well below the values of 25–30 and more commonly used on solar HALE aircraft; $AR = 14$ gives a good lift-to-drag ratio while keeping a shorter, stiffer wing with better control response. The span is therefore $b = \sqrt{(AR \cdot S)} = 10.25$ m, and the mean geometric chord $\bar{c} = S/b \approx 0.73$ m. The fuselage length was set at $L \approx 4.2$ m (about 41% of the span). In the present layout, the wing tapers from a root chord of 0.88 m to a tip chord of 0.60 m and uses a NACA 4412 section; both are representative choices, not requirements. The NACA 4412 was used because it is a well-documented section that also serves as a validation case for RANS simulations near maximum lift [30], which allows the numerical results of Sect. 4.5 to be checked; the final airfoil, selected to reach the design $C_{L\max}$ of 1.4 (Sect. 4.4), will be determined in the detailed design.

The ailerons are sized according to common practice to cover about 22% of each semi-span at the tip and about 18% of the local chord. The first-order sizing of the patent application targets a roll rate of 45–55° s^{-1} [13]; strip theory and a vortex-lattice calculation give about 15–25° s^{-1} for these ailerons at 15–20° deflection, which is still several times the roll rate of solar HALE aircraft. About 30° s^{-1} would require ailerons over roughly one third of the semi-span with a quarter-chord flap; the aileron size will therefore be fixed in the detailed design, together with the gust and crosswind requirements. The tail was sized with the volume coefficients;

$$V_{\mathrm{H}} = S_{\mathrm{h}} I_{\mathrm{h}} / (S\bar{c}) \quad , \quad V_{\mathrm{V}} = S_{\mathrm{V}} I_{\mathrm{V}} / (Sb) \qquad \textbf{(2)}$$

where the tail arms I_{h} and I_{V} are measured from the aerodynamic centre of the wing to those of the tail surfaces. A first layout gave $V_{\mathrm{H}} = 0.26$ and $V_{\mathrm{V}} = 0.011$, well below the typical values for sailplanes ($V_{\mathrm{H}} = 0.50$, $V_{\mathrm{V}} = 0.02$) and homebuilt aircraft ($V_{\mathrm{H}} = 0.50$, $V_{\mathrm{V}} = 0.04$) [29, Table 6.4]. The tail was therefore enlarged. Because the wing was later moved aft to obtain a statically stable centre-of-gravity position (Sect. 3.4), which shortens the tail arms, the final tail has $S_{\mathrm{h}} = 1.27$ m² (span 3.12 m, $I_{\mathrm{h}} = 1.84$ m) and $S_{\mathrm{V}} = 0.91$ m² (height 1.32 m, $I_{\mathrm{V}} = 1.69$ m), which gives $V_{\mathrm{H}} \approx 0.41$ and $V_{\mathrm{V}} \approx 0.020$ (Table 5).

Table 5. Geometry summary (model values; * representative, not specified in the patent application)

Parameter	Value	Source
Wing area S / span b / aspect ratio AR	7.5 m² / 10.25 m / 14	Sizing, [13]
Mean geometric chord $\bar{c}$	0.73 m	Sizing, [13]
Root/tip chord, taper	0.88 m / 0.60 m*	Layout
Dihedral (outboard of y = 0.9 m)	4°*	Layout
Fuselage length L	4.20 m	Sizing, [13]
PV area (upper wing)	6.40 m² (85% of S)	Model, [13]: 6.375 m²
Ailerons	22% semi-span, 18% chord	Sizing, [13]
Wing root leading edge behind the nose	1.55 m*	Layout (Sect. 3.4)
Horizontal tail S_{h}, span, V_{H}	1.27 m², 3.12 m*, 0.41	Layout
Vertical tail S_{V}, height, V_V	0.91 m², 1.32 m*, 0.020	Layout
Main-gear track/wheel diameter	1.60 m / 0.40 m	Layout
Propeller diameter	0.80 m*	Layout

The vertical tail thus matches the sailplane value, while V_{H} remains about 20% below it; since the values in [29] are conservative averages intended for initial sizing, the adequacy of the horizontal tail is confirmed by the static margin of 14.3% obtained from the three-dimensional CFD analysis (Sect. 4.6).

3.4. Internal arrangement and centre of gravity

Figure 5 shows the baseline internal arrangement. Its purpose is to show that the components of Table 4 fit into the airframe with a statically stable centre-of-gravity position; the final arrangement will be determined in the prototype design. The arrangement follows four rules. First, the positions defined in the patent application [13] are retained: the sensor bay (1a) in the nose, the mapping bay (1c) and the fuselage intake mouth (1b) on the lower mid-fuselage in line with the wing root, the intakes (2b) on the lower wing surface near the root and the ducts (2c) inside the wing. Second, the heavy components are placed close to the centre of gravity, and the hydrogen vessel, whose contents are consumed in flight, is placed so that the centre of gravity moves as little as possible during the mission. Third, the air, hydrogen, and electrical paths are kept short: the fuel-cell stack (5a) lies between the two ducts (2c) directly behind the hydrogen vessel, and the battery (5b) and the power distribution unit share the forward electronics bay.

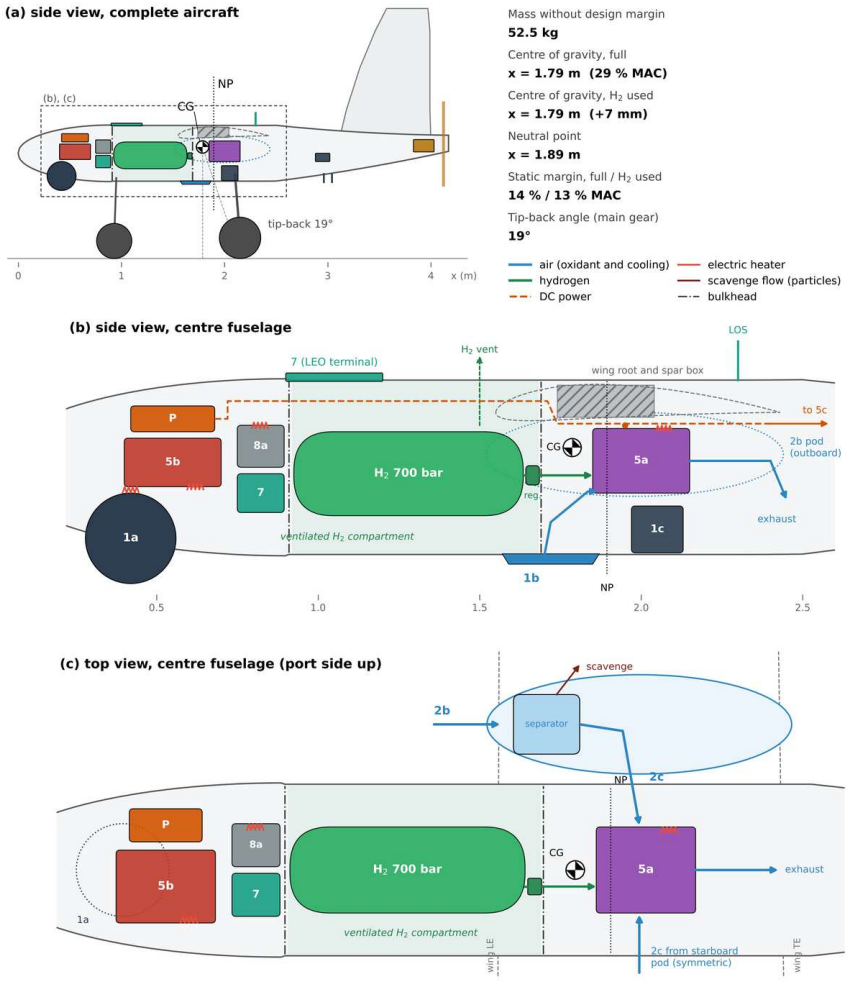


Figure 5. Baseline internal arrangement: **(a)** complete aircraft with centre of gravity (CG), neutral point (NP) and tip-back angle; **(b)** side view and **(c)** top view of the centre fuselage with the air, hydrogen, and DC paths. P: power distribution unit; bulkheads dash-dotted. Masses and positions are listed in Table 6. The final arrangement will be determined in the prototype design.

Fourth, the hydrogen vessel is housed in a separate, ventilated compartment between two bulkheads, with a vent on top and a hydrogen detector (Fig. 3), away from the battery and the electronics. At 70 MPa and 15 °C, hydrogen has a density of about 40 kg/m³ [31], so the 0.72 kg of Sect. 3.7 occupies about 18 *L*. A Type IV vessel with an outer diameter of 0.26 m, a length of 0.71 m, and an internal volume of about 20 *L* therefore fits the fuselage cross-section of 0.54 m, with room for the intake duct below it.

Table 6 lists the masses and positions. The centre of gravity and the tip-back angle were computed from these values with a Python script. Without the design margin, the aircraft has a mass of 52.45 kg and a centre of gravity 1.79 m behind the nose, at 29% of the mean aerodynamic chord; it moves 7 mm aft when the hydrogen has been consumed. In the first layout, with the wing root leading edge 1.15 m behind the nose, the centre of gravity lay behind the neutral point, mainly because the pusher motor, the propeller and the tail are at the rear of the fuselage. The wing, the wing-root intakes and the main landing gear were therefore moved 0.40 m aft, and the tail was enlarged to keep its volume coefficients (Sect. 3.3). With the neutral point from the three-dimensional RANS simulation (Sect. 4.6), x = 1.89 m, the static margin is about 14% of the mean aerodynamic chord with full hydrogen storage and 13% with the hydrogen consumed, so the aircraft is statically stable in pitch throughout the mission, with enough margin to accommodate the centre-of-gravity shifts of optional payloads.

Table 6. Masses and longitudinal positions of the components in the baseline arrangement (x, measured from the nose)

Component	Mass (kg)	x (m)
Wing structure incl. spar box	8.60	1.87
Fuselage structure	6.40	1.93
Horizontal and vertical tail	3.00	3.66
Fuel-cell stack and balance of plant (5a)	3.00	2.00
H_2 vessel, 70 MPa, incl. regulator and 0.72 kg H_2	9.00	1.28
Battery pack (5b)	7.20	0.55
Motor and ESC (5c)	2.80	3.95
Propeller (5c)	0.80	4.15
Power distribution, DC–DC converters (P)	1.00	0.55
Wiring, heaters, actuators	2.00	1.80
PV array (2a, 3a)	2.55	1.95
Main landing gear (4b)	1.80	2.15
Nose landing gear (4a)	0.60	0.93
Gimbal turret (1a)	0.40	0.42
LiDAR/RGB mapping unit (1c)	0.91	2.05
406 MHz direction finder (1d)	0.30	2.95
LEO satellite terminal (7)	1.10	1.05
LOS radio and Iridium modem (7)	0.34	0.83
Flight computer, IMU, GNSS/RTK (8a)	0.65	0.83
Total without design margin; centre of gravity	**52.45**	**1.79**
Centre of gravity with the hydrogen consumed	51.73	1.79

Mean aerodynamic chord 0.749 m, leading edge at x = 1.573 m; neutral point from the three-dimensional RANS simulation of Sect. 4.6: x = 1.89 m

If the design margin of 7.55 kg is used for an optional payload in the nose bay ($x \approx 0.6$ m), the centre of gravity moves forward to about 1.64 m, and the static margin increases to about 34%, which would require more elevator deflection for trim; heavier optional payloads are therefore better placed near the centre of gravity, where they change it only slightly. The main wheels (4b), 2.15 m behind the nose, give a tip-back angle of about 19°, above the minimum of about 15° commonly recommended for tricycle landing gear [29, Sect. 11.2].

3.5. Power required

The power required in steady level flight follows from the classical relations

$$C_{\mathrm{L}} = 2W/(\rho V^2 S) \quad , \quad C_{\mathrm{D}} = C_{\mathrm{D0}} + C_{\mathrm{L}}^2/(\pi ARe) \quad , \quad P_{\mathrm{el}} = DV/\eta = 1/2\rho V^3 S C_{\mathrm{D}}/\eta \qquad \textbf{(3)}$$

with W = 588.6 N, a zero-lift drag coefficient $C_{\mathrm{D0}} \approx 0.025$ (a conservative first-order estimate that includes the intake and payload protrusions), an Oswald factor e = 0.8 and a combined motor and propeller efficiency η = 0.75. At the cruise speed of 25 m/s, this gives $C_{\mathrm{L}} \approx 0.251$, $C_{\mathrm{Di}} \approx 0.0018$, $C_{\mathrm{D}} \approx 0.0268$, $D \approx 62.8$ N, an ideal propulsive power of about 1,570 W, and an electrical power of $P_{\mathrm{el}} \approx 2{,}093$ W. At the loiter speed of 18 m/s, $C_{\mathrm{L}} \approx 0.485$, $C_{\mathrm{Di}} \approx 0.0067$, $C_{\mathrm{D}} \approx 0.0317$, $D \approx 38.5$ N, about 692 W of propulsive power and $P_{\mathrm{el}} \approx 923$ W. With $C_{\mathrm{Lmax}} \approx 1.4$ for a simple flapless wing, the stall speed is about 10.6 m/s (38 km/h), which is favourable for short, rough strips. These values are checked independently in Sect. 4.

3.6. Solar energy yield

If 85% of the wing area is covered, the PV area is 0.85 × 7.5 = 6.375 m². With an assumed cell efficiency of 31% at standard test conditions (STC, 1,000 W/m²), consistent with multi-junction thin-film cells, the peak output is about 1,976 W, i.e., 94% of the cruise power requirement. With an areal mass of about 0.4 kg/m² including lamination and integration, the array mass is about 2.55 kg (Table 4).

Peak power alone does not say how much energy the array delivers over a day, which depends strongly on latitude and season. The daily yield was therefore estimated with the Ineichen–Perez clear-sky model [32] as implemented in pvlib Python (version 0.16) [33], with its built-in monthly Linke-turbidity climatology, for a horizontal wing at 2,000 m altitude and in 1-min steps. A system factor of 0.85 was applied for MPPT and conversion losses, encapsulation, wing curvature, temperature, and mismatch (an assumption). Two locations represent the ends of the operating envelope: Sabha, Libya (27.0° N, 14.4° E) and Ny-Ålesund, Svalbard (78.9° N, 11.9° E), each at the equinoxes and solstices. The demand is the loiter power of 923 W, plus 125 W of heating (the middle of the 100–150 W range of Sect. 2.4) for the Arctic case.

Table 7. Clear-sky daily PV energy and fuel-cell energy requirement at loiter

Location, date	Sun (h)	PV energy (kWh)	PV peak (W)	Demand (kWh)	FC energy (kWh)	PV share
Sabha, 20 March	12.1	12.6	1748	22.2	13.5	39%
Sabha, 21 June	13.8	15.4	1899	22.2	12.2	45%
Sabha, 21 December	10.4	7.6	1228	22.2	15.5	30%
Ny-Ålesund, 20 March	12.3	1.8	274	25.2	23.3	7%
Ny-Ålesund, 21 June	24.0	16.1	1040	25.2	9.1	64%
Ny-Ålesund, 21 December	0.0	0.0	0	25.2	25.2	0%

Horizontal wing at 2,000 m, clear sky, Ineichen–Perez model [32] in pvlib [33]; PV area 6.375 m², cell efficiency 31%, system factor 0.85. Demand: 923 W (Sabha) and 923 + 125 W (Ny-Ålesund). September values are within 0.2 kWh of March.

The energy that the fuel cell must supply is the daily integral of max (0, $P_{\mathrm{req}} - P_{\mathrm{PV}}$); surplus PV energy is not stored, which is conservative. The results are listed in Table 7, and the daily profiles are shown in Fig. 6.

In the Libyan desert, the array delivers about 15.4 kWh on a clear summer day and 7.6 kWh in midwinter; it carries the whole loiter load for about 8.6 h in June and covers 45% (June) to 30% (December) of the 24-h demand. At Ny-Ålesund, the midnight sun gives the largest daily energy of all cases, 16.1 kWh, and covers 64% of the demand, but the low sun limits the peak to about 1040 W, so the array never carries the whole load alone. At the equinox, the Arctic yield drops to 1.8 kWh (7%), and during the polar night it is zero, so the aircraft relies entirely on hydrogen. This is exactly the situation the tri-source architecture is designed for. Because the model assumes clear skies, these values are upper bounds; clouds will reduce them.

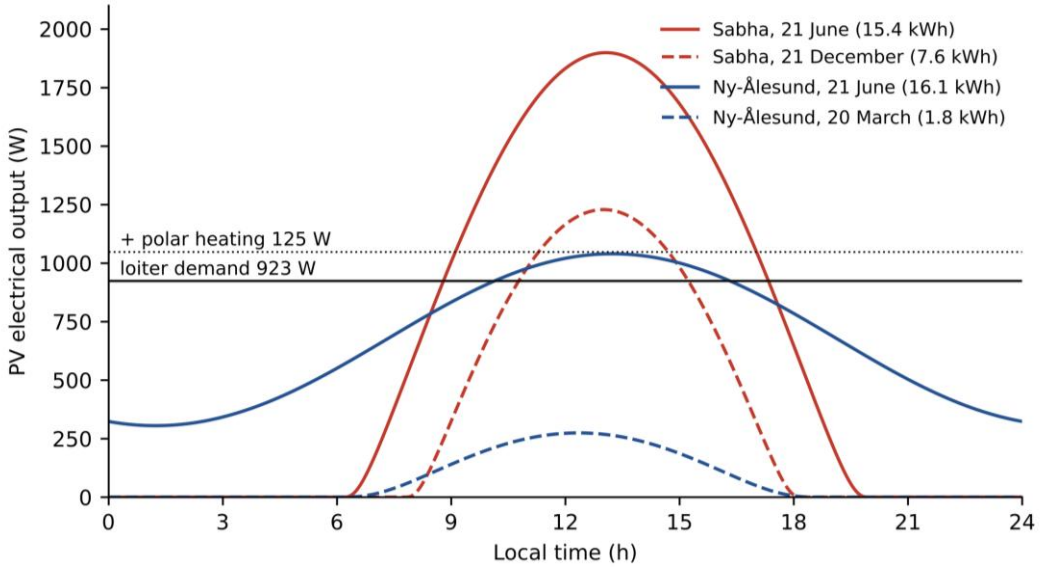


Figure 6. Clear-sky PV output over one day for the two locations, compared with the loiter power demand. Daily PV energy in parentheses.

3.7. Hydrogen energy and endurance

Of the 12 kg allotted to the fuel-cell stack and hydrogen storage, the hydrogen mass follows from the gravimetric efficiency of the storage, defined as hydrogen mass divided by total storage mass including hydrogen. Taking 5–7% with a mean of 6% gives 12 × 0.06 = 0.72 kg of hydrogen. For comparison, first calculations by Hüppauff et al. indicate that a gravimetric efficiency of about 7.4%, defined in the same way, is realistic for a novel load-bearing composite pressure vessel integrated into an aircraft wing [12]. With a lower heating value of 33.3 kWh/kg and a fuel-cell system efficiency of about 50%, the usable electrical energy is 0.72 × 33.3 × 0.5 ≈ 12.0 kWh.

On hydrogen alone, the endurance is therefore 12,000/2,093 ≈ 5.7 h at full cruise power and 12,000/923 ≈ 13.0 h at loiter. Since most observation and mapping is flown at loiter speed, the operational night endurance approaches 13 h. In the polar case, the heating loads of Sect. 2.4 (100–150 W) must be added: the loiter load becomes 1,023–1,073 W and the endurance 11.2–11.7 h; at cruise it becomes 5.35–5.5 h. The battery (7.2 kg, about 200 Wh/kg, ≈ 1.44 kWh) is not a primary endurance source; it buffers load peaks and supplies the fuel-cell pre-heating circuit.

Combining hydrogen with the PV yield of Sect. 3.6 extends the endurance considerably. Averaged over the diurnal cycle, 12.0 kWh of hydrogen covers the fuel-cell share of about 23.6 h of loiter at Sabha in June and 18.6 h in December, about 31.7 h at Ny-Ålesund in June, and 11.5 h in the polar night (hydrogen only, including heating). These clear-sky figures are upper bounds; the actual values also depend on the launch time.

The first-order calculation also shows a physical limit that is acknowledged openly. Uninterrupted 24-h flight at full cruise power on hydrogen alone would require about 24 × 2,093 W ≈ 50 kWh, i.e., about 3.0 kg of hydrogen at an electrical yield of 16.65 kWh/kg, which at 6% gravimetric efficiency means about 50 kg of hydrogen plus storage, or about 84% of MTOW. Months-long flight in the style of Zephyr or PHASA-35 is therefore not possible in this mass class. The realistic and defensible target is a single sortie with about 11.5–13 h of night or sunless loiter reserve, extended by the PV array in daylight, followed by return to base for refuelling.

4. Aerodynamic assessment

4.1. Methods

The design estimates of Sect. 3.5 were checked independently with the open-source framework AeroSandbox (version 4.2) [34]. A vortex lattice method (VLM) was applied to the isolated wing to obtain the lift-curve slope and the inviscid span efficiency. Two-dimensional section polars were computed with NeuralFoil [35] (version 0.3, large model) at the Reynolds numbers of the stall, loiter, and cruise speeds. The drag of the complete aircraft (wing, horizontal and vertical tail, fuselage and the two intake pods) was computed with the AeroBuildup component drag build-up of AeroSandbox; for each speed the angle of attack was adjusted until the lift equalled the weight. The atmosphere was the ISA at 2,050 m (ρ = 1.0 kg/m³), and the Reynolds numbers based on the mean chord are 0.45 × 10^6 at 10.6 m/s, 0.77 × 10^6 at 18 m/s, and 1.07 × 10^6 at 25 m/s. AeroBuildup does not include protrusions such as the landing gear, the gimbal sphere, and the antennas; their drag was added separately with typical drag coefficients [36] as a low and a high estimate (Appendix A). The sizing equations of Sect. 3, the centre-of-gravity and solar-yield calculations, the separator estimate of Sect. 6.5, and the post-processing of all simulations were implemented in Python 3.13 with NumPy, SciPy and Matplotlib.

4.2. Geometry and assumptions

The geometry is that of the three-dimensional model of Figs. 1 and 2: a wing with root chord 0.88 m and tip chord 0.60 m, a dihedral break at y = 0.9 m with 4° outboard, NACA 4412 sections on the wing and NACA 0009 on the tail surfaces, a fuselage of 0.27 m maximum radius and the resized tail of Sect. 3.3. The intake pods were modelled as bodies of revolution. Because the wing tips are not rounded in the AeroSandbox model, its reference area is 7.60 m² (7.52 m² in the 3-D model and 7.5 m² in the sizing); this 1.3% difference does not materially affect the results. The internal flow and cooling drag of the intakes were not modelled.

4.3. Results

The VLM gives a lift-curve slope of 5.29 rad^{-1} and an inviscid span efficiency of 0.99 at $C_L \geq 0.33$ (0.94 at C_L = 0.15). The value e = 0.8 used in the sizing is therefore conservative; the inviscid value is an upper bound on the real Oswald factor, which also includes viscous drag due to lift. NeuralFoil gives maximum section lift coefficients of 1.46, 1.55 and 1.60 for the NACA 4412 at

Re = 0.45, 0.77 and 1.07 × 10^6 (Fig. 7). With the usual first-order knock-down of 0.9 for an unswept, flapless, high-aspect-ratio wing, C_{Lmax} ≈ 1.31 and the stall speed is about 10.9 m/s.

For the clean airframe, AeroBuildup gives a drag coefficient of 0.0138 near zero lift. The protrusions add 0.0068–0.0140 (Appendix A), so the zero-lift drag coefficient of the complete aircraft lies between about 0.021 and 0.028. At cruise (C_{L} = 0.248, α ≈ −2.0°), the clean drag coefficient is 0.0146, and the total is 0.022–0.029; at loiter (C_{L} = 0.478, α ≈ +0.2°), it is 0.0192 and 0.026–0.033. The negative angle of attack at cruise indicates that the wing should be set at an incidence of about +2° relative to the fuselage datum so that the fuselage flies level in cruise. The resulting electrical power is 1,700–2,270 W at cruise and 770–980 W at loiter (Fig. 8), and the hydrogen-only endurance with 12.0 kWh is 5.3–7.1 h and 12.2–15.6 h, respectively.

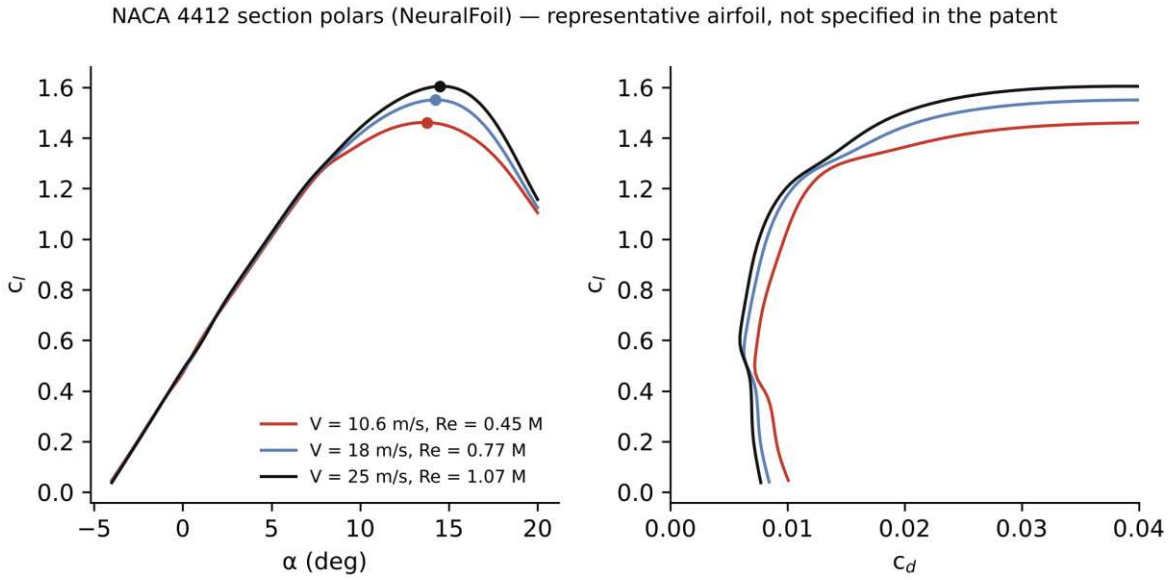


Figure 7. NACA 4412 section polars from NeuralFoil at the Reynolds numbers of the stall, loiter, and cruise speeds. The airfoil is a representative choice.

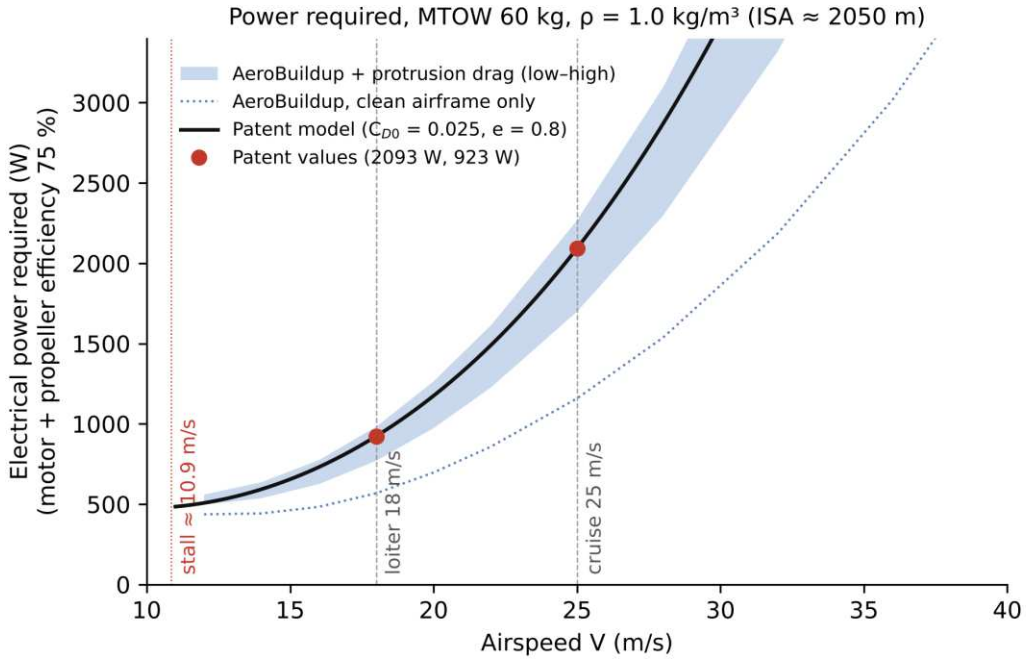


Figure 8. Electrical power required versus airspeed. Black: design model of Sect. 3.5 (C_{D0} = 0.025, e = 0.8); blue band: AeroBuildup plus protrusion drag (low–high); dotted: clean airframe only; red points: design values at loiter and cruise.

4.4. Comparison with the design estimates

Table 8 compares the first-order design values with the results of the low-fidelity analysis. All power and endurance values of the design lie inside the computed ranges; the design C_{D0} of 0.025 lies in the middle of the computed range of 0.021–0.028. The only value outside the computed range is the maximum lift coefficient: the design value of 1.4 would require an airfoil with somewhat higher maximum lift than the NACA 4412 assumed here, and the corresponding stall speed is 10.9 m/s instead of 10.6 m/s.

Table 8. Design values (Sect. 3) compared with the low-fidelity analysis (Sect. 4)

Quantity	Design (Sect. 3)	Analysis (Sect. 4)
Zero-lift drag , C_{D0}	0.025	0.0138 (clean); 0.021–0.028 (with protrusions)
Oswald factor, e	0.8	0.99 (inviscid VLM, upper bound)
Cruise, C_L (25 m/s)	0.251	0.248
Cruise electrical power	2,093 W	1,700–2,270 W
Loiter electrical power (18 m/s)	923 W	770–980 W
Endurance on H_2, cruise	5.7 h	5.3–7.1 h
Endurance on H_2, loiter	13.0 h	12.2–15.6 h
C_{Lmax} (3-D)	1.4	≈ 1.31 (NACA 4412, Re = 0.45 × 10^6)
Stall speed	10.6 m/s	10.9 m/s

4.5. Two-dimensional RANS simulations

To complement the low-fidelity assessment, two-dimensional Reynolds-averaged Navier–Stokes (RANS) simulations were carried out for the wing section and for the vane row of the intake separator. The steady incompressible equations were solved with OpenFOAM v1912 [37] using the SIMPLEC algorithm, second-order linear-upwind discretisation of the convective terms, and the k–ω SST turbulence model [38], integrated down to the wall without wall functions. Hybrid meshes were generated with Gmsh 4 [39]: layers of quadrilateral cells resolve the boundary layer with a dimensionless wall distance y^+ below 1, triangles fill the remainder of the domain, and a single cell in the spanwise direction makes the problem two-dimensional. The integral quantities were evaluated after 3,000 iterations; for selected cases, the iteration count was doubled without any change in the results to four significant digits. Lift, drag, and pitching moment were obtained by integrating the wall pressure and the wall shear stress with Python post-processing scripts.

***Wing section*.** The NACA 4412 section was simulated at the loiter Reynolds number of 0.77 × 10^6 for angles of attack between −4° and 16°, in a circular domain with a radius of 25 chords and about 63,500 cells, with a first cell height of 1 × 10^{-5} chords. Because the SST model treats the boundary layer as fully turbulent, the results are compared in Fig. 9 with NeuralFoil both for free transition, as used in Sect. 4.3 and Fig. 7, and with transition tripped at 1% of the chord.

The lift of the RANS simulations agrees closely with the tripped NeuralFoil results. The lift-curve slope between −4° and 8° is 5.82 per radian compared with 5.97 per radian, the zero-lift angle is −4.1° compared with −4.2°, and up to 10° the two lift curves differ by at most 0.04. With free transition, NeuralFoil predicts a slightly higher lift (slope 6.09 per radian, zero-lift angle −4.5°), because the thinner laminar boundary layer reduces the decambering effect of the viscous layer near the trailing edge. Near the stall, the methods diverge: the RANS lift still rises to 1.64 at 16°, whereas NeuralFoil gives a maximum of about 1.55 at 14° with both free and tripped transition. Steady RANS with eddy-viscosity models tends to underpredict the trailing-edge separation of this section, so the lower NeuralFoil value is retained for the stall

speed in Sect. 4. In the attached-flow range used for cruise and loiter, the section lift data of Sect. 4 are thus confirmed by an independent method.

The drag depends strongly on the transition location. At a section lift coefficient of 0.5, which corresponds to loiter, the profile drag coefficient is 0.0066 with free transition, 0.0125 with transition tripped at 1% of the chord, and 0.0137 for the fully turbulent RANS solution. Early transition of this kind is plausible if the encapsulation and the edges of the PV panels act as roughness near the leading edge. The difference between free and fully turbulent flow, $\Delta C_{\mathrm{d}} \approx 0.0071$, would increase the loiter power by up to about 208 W and reduce the hydrogen-only loiter endurance with the heating load from 11.4 to about 9.5 h. Keeping the panel edges and the encapsulation smooth over the forward part of the wing is therefore a design requirement, and the transition location should be checked in the wind tunnel, for example by oil-flow or infrared visualisation.

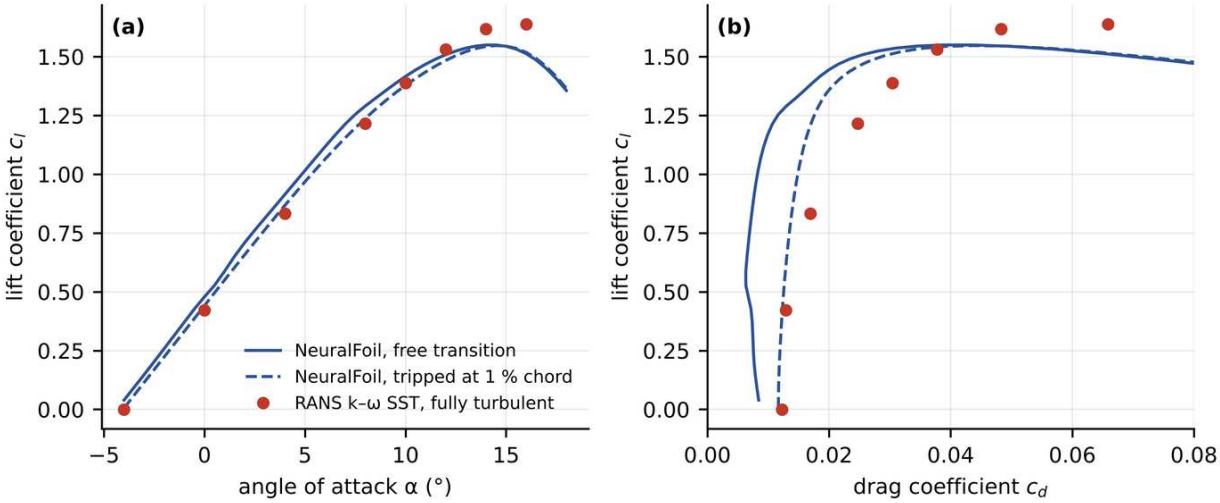


Figure 9. NACA 4412 at $Re = 0.77 \times 10^6$: **(a)** lift coefficient versus angle of attack and **(b)** drag polar. Red symbols: RANS simulations with the *k–ω* SST model (fully turbulent); blue lines: NeuralFoil with free transition (solid) and with transition tripped at 1% of the chord (dashed).

Separator vane row. The vane row of the separator (Sect. 2.3) was modelled as a two-dimensional linear cascade, that is, as a cut through the vane row at mid-radius developed into a plane, with translational periodicity between neighbouring passages. The vanes have a circular-arc camber line with an axial inlet angle and exit (metal) angles β of 30°, 45° and 60°, a NACA four-digit thickness distribution of 6% and a chord of 30 mm, at a solidity of 1. With an axial inlet velocity of 20 m/s, the chord Reynolds number is 4×10^4. The inlet lies 1.5 chords upstream of the leading edge and the outlet 3 chords downstream of the trailing edge; the inlet turbulence intensity is 2%, and the meshes have about 18,000–19,000 cells. The exit flow angle α_2 was evaluated as the mixed-out angle from the pitch-integrated fluxes of mass and tangential momentum, and the loss as the drop of the mass-averaged total pressure, $Y = \Delta p_0 / q_{\mathrm{ax}}$, both one chord behind the trailing edge. The results are listed in Table 9, and the flow fields are shown in Fig. 10.

For all three vane angles, the flow remains attached and leaves the vane row as a uniform, turned stream (Fig. 10). The flow is turned by 7–14° less than the vane angle, which is the deviation familiar from turbomachinery cascades, so that the exit flow angles are 23.1°, 34.6° and 45.6°. The deviation is of the order given by Carter's rule for circular-arc cascades [40], which, having been derived for decelerating compressor cascades, tends to overestimate it for an accelerating vane row such as this one. As required by the conservation of tangential momentum in a periodic cascade, the mixed-out exit angle does not change between 0.5 and

2 chords behind the trailing edge. Refining the mesh by a factor of about 1.8 changes the exit angle by less than 0.25° and the loss coefficient by less than 4%, and halving the inlet velocity to 10 m/s (Re = 2 × 10^4) reduces the exit angle at β = 45° by 0.6° and increases the loss coefficient from 0.040 to 0.052.

Table 9. Two-dimensional RANS results for the separator vane row (chord 30 mm, solidity 1, axial inlet velocity 20 m/s, Re = 4 × 10^4)

Vane angle β	Exit flow angle α_2	Deviation $\beta - \alpha_2$	Loss coefficient Y	Static-pressure drop $\Delta p/q_{ax}$	Fine mesh α_2 / Y
30°	23.1°	6.9°	0.027	0.21	23.1° / 0.026
45°	34.6°	10.4°	0.040	0.52	34.4° / 0.039
60°	45.6°	14.4°	0.069	1.11	45.4° / 0.066

$q_{ax} = 1/2\rho V_{ax}^2$, evaluated one chord behind the trailing edge. The fine meshes have about 1.8 times as many cells.

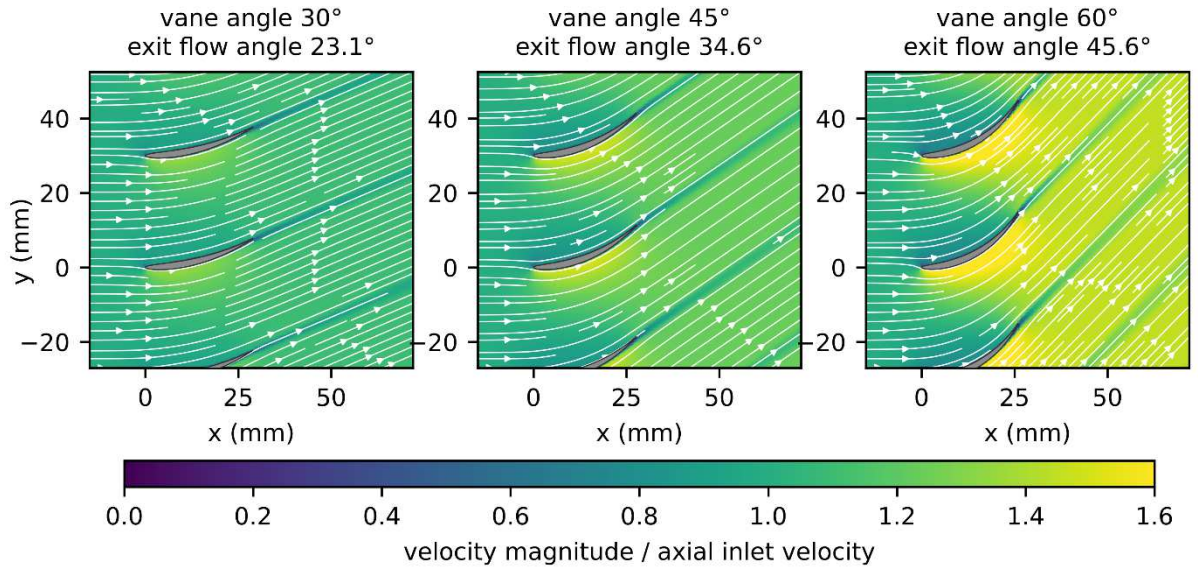


Figure 10. Two-dimensional RANS simulation of the separator vane row for vane angles of 30°, 45° and 60°: velocity magnitude relative to the axial inlet velocity of 20 m/s, with streamlines. Two passages of the periodic cascade are shown; the exit flow angle is given above each panel.

Two results are relevant to the design. First, the irreversible loss of the vane row is small, with loss coefficients of 0.027–0.069, but the static pressure falls by 0.21, 0.52, and 1.11 times the axial dynamic pressure, because the swirl itself carries kinetic energy ($\Delta p/q_{ax} \approx \tan^2\alpha_2 + Y$). Unless this energy is recovered by de-swirling vanes or a diffuser downstream of the separator, it has to be supplied by the ram pressure. Second, the centrifugal separation is governed by the exit flow angle rather than by the vane angle; Sect. 6.5 therefore uses the computed exit angles.

4.6. Three-dimensional RANS simulation of the complete aircraft

The clean configuration of the aircraft, consisting of fuselage, wing and horizontal and vertical tail without landing gear, intakes, propeller and sensor turret, was simulated as a half model with a symmetry plane, at the loiter speed of 18 m/s in the ISA at 2,050 m (Re = 0.77 × 10^6 based on the mean chord). The same solver and turbulence model as in Sect. 4.5 were used, here with a wall function that is valid in both the viscous sublayer and the logarithmic layer. The geometry is that of Figs. 1 and 2 with closed surfaces. Hex-dominant meshes with four prism layers on all walls were generated with the blockMesh and snappyHexMesh utilities of OpenFOAM in a domain extending 12 m upstream, 26 m downstream, 20 m laterally and 15

m above and below the aircraft. Three meshes with 0.13, 0.36 and 0.98 million cells, refined systematically by a factor of about 1.4 in cell size, were used at α = 4° to estimate the discretisation uncertainty with Richardson extrapolation and the grid convergence index (GCI) [41]; the fine mesh was then used at α = 0°. The median y^+ on the wing of the fine mesh is about 39.

Table 10. Mesh convergence of the three-dimensional RANS results at α = 4° and 18 m/s (clean configuration).

Mesh	Cells (millions)	C_L	C_D	C_m
Coarse	0.13	0.540	0.0806	–0.174
Medium	0.36	0.649	0.0456	–0.153
Fine	0.98	0.684	0.0361	–0.144
Extrapolated (p = 2)	–	0.720	0.0260	–0.135
GCI of fine mesh	–	7%	35%	8%

Moment reference point 1.73 m behind the nose (about 25% of the mean chord). Reference area 7.5 m², reference chord 0.73 m.

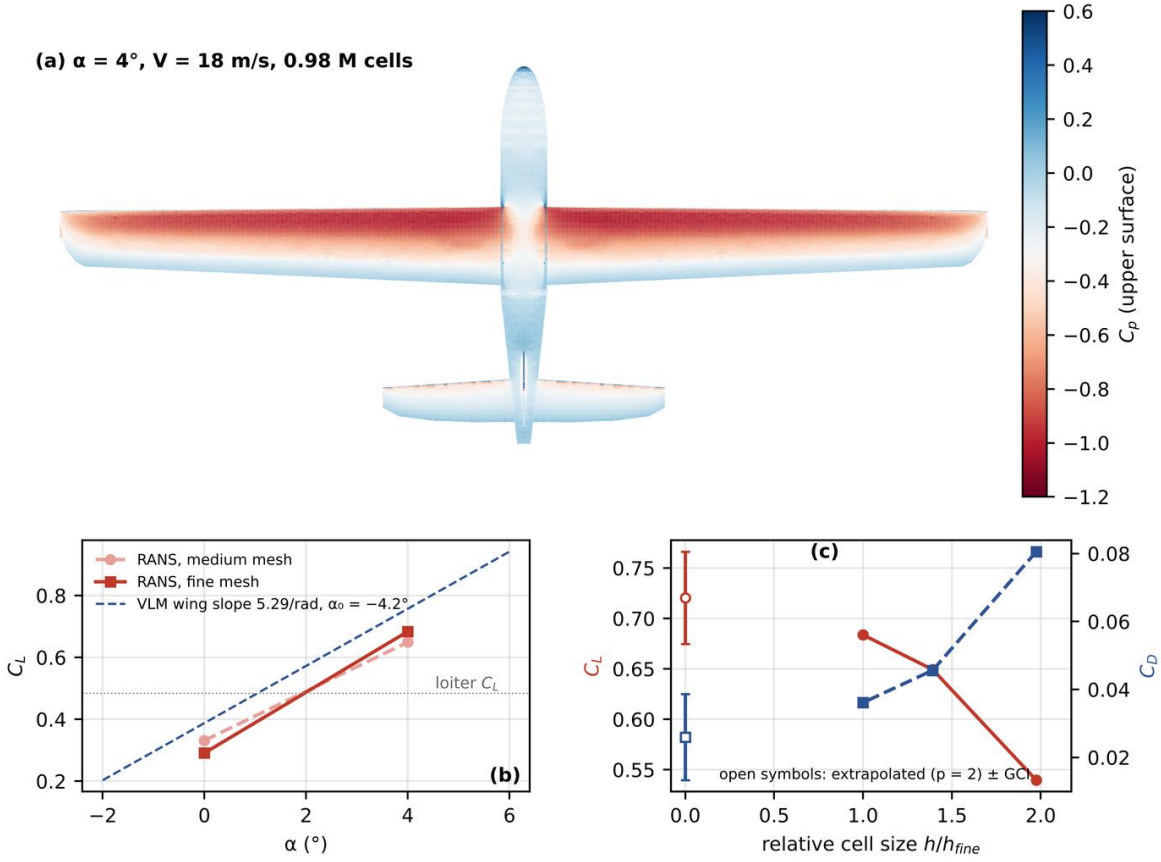


Figure 11. Three-dimensional RANS simulation of the clean configuration at 18 m/s: **(a)** pressure coefficient on the upper surfaces at α = 4° (fine mesh); **(b)** lift coefficient versus angle of attack, with the inviscid slope of the isolated wing for comparison; (c) lift and drag coefficients at α = 4° versus the relative cell size of the three meshes.

The lift converges monotonically with mesh refinement (Table 10). The fine-mesh value at α = 4° is C_L = 0.684, and the extrapolated value is 0.720 with a grid convergence index of 7%. Between α = 0° and 4°, the fine mesh gives a lift-curve slope of 5.63 per radian and a zero-lift angle of −3.0°. The wing alone contributes 4.89 per radian, about 8% less than the inviscid vortex-lattice slope of the isolated wing (5.29 per radian, Sect. 4.3), as expected from the viscous decambering of the section (Sect. 4.5); the horizontal tail and the fuselage provide the remainder, and the wing carries 94% of the lift at α = 4°. The lift coefficient of 0.484 required

at loiter is reached at $\alpha \approx 2.0°$, so the aircraft loiters with a moderate fuselage incidence and a large margin to the stall.

The drag converges more slowly: the fine-mesh value at α = 4° is 0.0361, and Richardson extrapolation gives 0.0260 with a grid convergence index of 35%. At the loiter lift coefficient, the fine mesh gives $C_D \approx 0.0295$, compared with 0.0192 from the component build-up of Sect. 4.3 for the clean airframe including the two intake pods. The difference is mainly numerical pressure drag, which decreases with every refinement; the three-dimensional simulation therefore confirms the lift and the trim condition, whereas the drag estimate of Sect. 4.3 remains the reference until finer meshes or wind-tunnel data are available. The pitching moment decreases with lift, $\mathrm{d}C_\mathrm{m}/\mathrm{d}C_\mathrm{L} \approx -0.22$, which places the stick-fixed neutral point about 1.89 m behind the nose. With the centre of gravity of Sect. 3.4 (1.79 m), the static margin is about 14% of the mean aerodynamic chord with full hydrogen storage and 13% when the hydrogen has been consumed, so the baseline arrangement is statically stable in pitch throughout the mission. The pressure distribution and the results are shown in Fig. 11.

5. Planned experimental validation

The results of this paper are numerical. As a next step, an experimental campaign in three parts is planned. First, forces and moments of a 1:6 scale model of the complete aircraft (span 1.71 m) will be measured in a 2.5 m × 2.5 m closed-circuit test section at 40–60 m/s (Re = 0.3–0.5 × 10^6), in the clean configuration of Sect. 4.6 and with transition strips, open intakes, landing gear, and ski module, to determine $C_{\mathrm{L}\alpha}$, C_{Lmax}, C_{D0}, the Oswald factor, and the drag increments of these components. Second, a two-dimensional NACA 4412 model will be tested at $Re \approx 0.5 \times 10^6$ with free and fixed transition to quantify the profile-drag penalty identified in Sect. 4.5. Third, the exit flow angle and the total-pressure loss behind a full-scale linear cascade of the separator vanes will be measured with a five-hole probe for comparison with Table 9; the particle-separation efficiency will be determined separately in a duct rig with standardised test dust (ISO 12103-1). The results will be reported in a subsequent paper.

6. Discussion

6.1. Limitations of the present assessment

The aerodynamic assessment is deliberately low-fidelity. The VLM is inviscid; NeuralFoil and AeroBuildup assume clean surfaces, whereas the encapsulation of the PV cells, panel edges, and surface waviness may trigger earlier laminar–turbulent transition and increase the profile drag. Apart from the two-dimensional simulation of the vane row in Sect. 4.5, the internal flow, pressure loss and cooling drag of the intakes, the spillage drag at off-design conditions and the interaction of the pusher propeller with the fin and the fuselage wake are not included. The protrusion drag rests on handbook coefficients. The solar yield is a clear-sky upper bound for a horizontal wing. Finally, the tail was sized with volume coefficients and checked only for longitudinal static stability; dynamic stability and control have not yet been analyzed. These limitations are the reason for the planned wind-tunnel tests (Sect. 5) and for finer three-dimensional simulations that include the intakes, the landing gear, and the propeller.

6.2. Sensitivities

The most important aerodynamic uncertainty is the zero-lift drag. Across the computed range C_{D0} = 0.021–0.028, the hydrogen-only loiter endurance without heating load varies between 15.6 and 12.2 h, and the design value of 13.0 h lies at the conservative end of this range. Fairings on the main wheels would move the aircraft towards the lower end of the range,

whereas premature transition on the PV-covered wing would move it towards the upper end (Sect. 4.5). The second aerodynamic uncertainty is the maximum lift coefficient: with the NACA 4412 section, the stall speed is 0.3 m/s higher than assumed in the sizing, which is small for the intended short-field operations but should be resolved by the choice of the final airfoil.

The sizing of Sect. 3 also rests on many system-level assumptions, whose influence was examined with a one-at-a-time sensitivity analysis. For this purpose, the sizing equations of Sects. 3.5–3.7 were re-implemented in Python, and five parameters were varied individually while all others were held at their design values. The implementation reproduces the design values exactly, namely an electrical power of 2,093 W at cruise and 923 W at loiter, a usable hydrogen energy of 12.0 kWh, and a loiter endurance of 12.98 h without and 11.43 h with a heating load of 125 W. The output considered is the hydrogen-only loiter endurance including the heating load, since this is the quantity that governs night-time and polar operation. The results are summarised in Table 11 and Fig. 12.

Table 11. One-at-a-time sensitivity of the hydrogen-only loiter endurance (125 W heating load; design value 11.4 h)

Parameter	Range	Endurance at lower bound (h)	Endurance at upper bound (h)
H_2 storage gravimetric efficiency	4–8%	7.6	15.2
Flight speed (cruise and loiter scaled together)	0.8–1.2 × design	16.2	7.8
Wing loading	5–15 kg/m²	8.5	13.6
Heating load	0–200 W	13.0	10.7
Battery specific energy	150–350 Wh/kg	11.4	11.4

All other parameters at their design values (Sect. 3): MTOW = 60 kg, W/S = 8 kg/m², AR = 14, ρ = 1.0 kg/m³, C_{D0} = 0.025, e = 0.8, η = 0.75, 12 kg fuel-cell and storage mass, 6% gravimetric efficiency, fuel-cell system efficiency 50%.

The gravimetric efficiency of the hydrogen storage has the largest influence. Because the usable energy is proportional to the stored hydrogen mass, the endurance scales linearly with this efficiency: the range of 4–8% gives 7.6–15.2 h, and the range of 5–7% assumed in Sect. 3.7 gives 9.5–13.3 h. The storage technology is therefore the most effective single lever on endurance, which underlines the relevance of load-bearing and conformal pressure vessels for small aircraft [12].

Flight speed is the second driver: scaling the cruise and loiter speeds together by 0.8–1.2 changes the loiter endurance from 16.2 to 7.8 h. This result reflects the shape of the power curve and requires careful interpretation. With C_{D0} = 0.025 and e = 0.8, the lift coefficient for minimum power, $C_{\mathrm{L}} = \sqrt{3\pi AReC_{\mathrm{D0}}}$ ≈ 1.62, exceeds the assumed maximum lift coefficient of 1.4, so that the power required decreases monotonically down to the stall speed (Fig. 8). The loiter speed of 18 m/s, about 1.7 V_{s}, is therefore not the speed of minimum power. It is a deliberate margin against gusts and low-level turbulence, and it keeps the aircraft well away from the stall in the density and temperature extremes discussed in Sect. 6.3. If the parabolic drag polar remained valid at higher lift coefficients, loitering at 1.3 V_{s} (about 13.8 m/s) would require about 580 W and extend the endurance to about 17 h with the heating load. Since the profile drag of a real section rises at high lift coefficients (Fig. 9b) and the margin to the stall becomes smaller, this potential should be quantified with the drag polar measured in the wind tunnel (Sect. 5) before the loiter speed is changed.

Wing loading has a smaller influence, with 5–15 kg/m² giving 8.5–13.6 h. A lower wing loading means a larger wing for the same mass, which lowers the stall speed and enlarges the area available for the PV array but increases the parasite drag; a higher wing loading has the opposite effect and raises the stall speed to 14.5 m/s at 15 kg/m². Because the take-off mass

and the structural mass are kept constant in this analysis, the structural penalty of a larger wing and the solar energy lost with a smaller one are not captured, and the trend should be regarded as indicative.

The heating load has a comparatively small effect. Between 0 and 200 W the endurance varies from 13.0 to 10.7 h, so that even a doubling of the estimated 100–150 W would cost less than one hour. The specific energy of the battery has no direct effect on endurance in this architecture, because the battery serves as a power buffer and as the energy source for fuel-cell pre-heating rather than as an energy store for flight. Its effect is on the mass budget instead: with the buffer energy fixed at 1.44 kWh, an increase from 200 to 300 Wh/kg would reduce the battery mass from 7.2 to 4.8 kg, and if the 2.4 kg saved were added to the hydrogen storage at the same gravimetric efficiency, the loiter endurance would increase from 11.4 to about 13.7 h. A one-at-a-time analysis does not capture interactions between parameters, and the aerodynamic coefficients C_{D0} and e were held constant; their uncertainty is represented by the drag range of Sect. 4. A combined analysis, for example by Monte Carlo sampling, will become meaningful once these coefficients are based on wind-tunnel measurements.

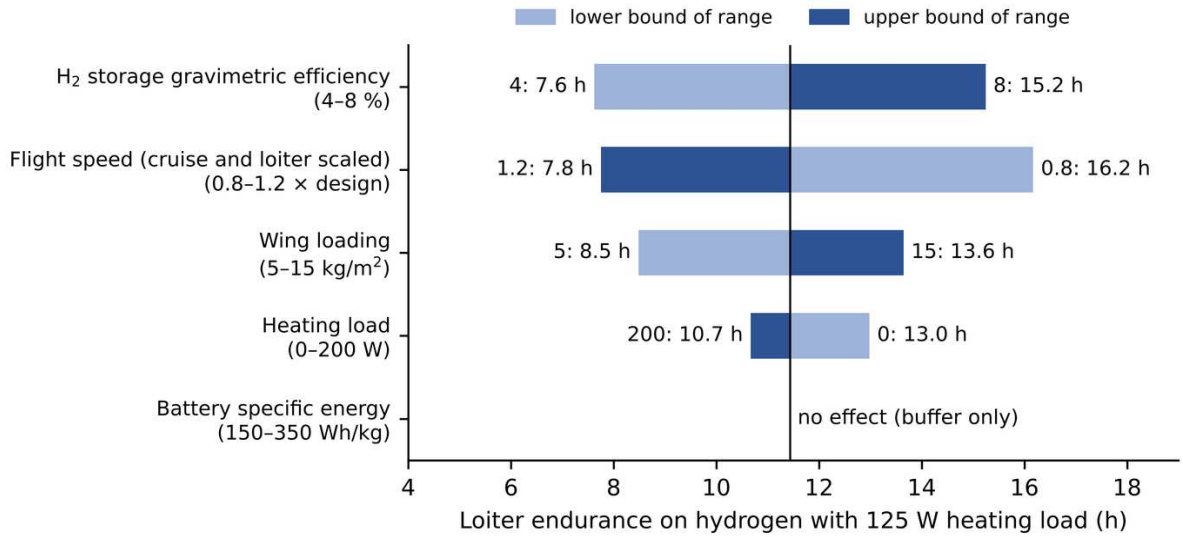


Figure 12. One-at-a-time sensitivity of the hydrogen-only loiter endurance with a heating load of 125 W to five design parameters. The vertical line marks the design value of 11.4 h; light bars correspond to the lower and dark bars to the upper bound of each parameter range.

6.3. Density, temperature and operating envelope

The sizing density of 1.0 kg/m³ corresponds to about 2,050 m in the ISA, not to sea level, where ρ = 1.225 kg/m³. If the aircraft flies at a constant lift coefficient (constant equivalent airspeed), the power required scales with $\rho^{-1/2}$. On a hot day at 2,000 m (ISA + 30 K, $\rho \approx 0.91$ kg/m³) the loiter power therefore rises by about 5% to roughly 970 W and the stall speed to about 11.5 m/s. At sea level and +50 °C ($\rho \approx 1.09$ kg/m³) the loiter power falls by about 4%, and in −50 °C air at sea level ($\rho \approx 1.58$ kg/m³) by about 20% to roughly 730 W, with a stall speed of about 8.7 m/s; in the cold case this saving partly offsets the 100–150 W heating load. The hot end is also the critical case for fuel-cell cooling, because the temperature difference available for heat rejection is smallest; the intake should therefore be sized for the hot case.

6.4. Intake air-flow budget

Section 2.3 shows that the intake must be sized for cooling rather than for oxidant supply, and that the dynamic pressure available at loiter is only about 160 Pa. The pressure loss of the swirl

vanes and the scavenge flow must therefore be small compared with this value, which is a key design target for the separator and should be measured in the wind tunnel.

6.5. Separator cut size and ram-pressure limit

The separation performance of the swirl separator can be estimated with the classical equilibrium-orbit (time-of-flight) model that is used for cyclones and for engine air particle separators [9]. If the flow leaves the vanes with a uniform tangential velocity $v_\theta = V_{\mathrm{ax}}\tan\alpha_2$, where V_{ax} is the axial velocity and α_2 is the exit flow angle, a particle subject to Stokes drag drifts outwards with

$$\mathrm{d}r/\mathrm{d}t = \tau_{\mathrm{p}} v_\theta^2 / r \quad , \quad \tau_{\mathrm{p}} = \left(\rho_{\mathrm{p}} d_p^2\right)/(18\mu) \qquad \textbf{(4)}$$

where τ_{p} is the particle relaxation time, ρ_{p} and d_{p} are the particle density and diameter, and μ is the dynamic viscosity of air. Integrating over the residence time $t_{\mathrm{res}} = L_{\mathrm{s}}/V_{\mathrm{ax}}$ in a swirl section of length L and radius R, and assuming that the particles are uniformly distributed over the cross-section, the fraction of particles that reaches the outer wall is

$$\eta_{\mathrm{s}}(d_p) = \min\left[1, 2\tau_{\mathrm{p}} v_\theta^2 t_{\mathrm{res}}/R^2\right] \qquad \textbf{(5)}$$

and the cut size d_{50} follows from $\eta_{\mathrm{s}} = 0.5$.

With the exit flow angles of Table 9, an illustrative separator with R = 20 mm, L_{s} = 100 mm and V_{ax} = 20 m/s has cut sizes for sand (ρ_{p} = 2,600 kg/m³) of 5.9, 3.6 and 2.5 µm for vane angles of 30°, 45° and 60°, and for water droplets of 9.5, 5.8 and 4.0 µm. Using the vane angle instead of the exit flow angle would give values about 30–40% smaller (4.3, 2.5 and 1.4 µm for sand). The model neglects radial swirl variation and particle re-entrainment at the wall, so the values are optimistic bounds, but they indicate that the separator can remove the sand and droplet sizes that dominate erosion and water ingestion, consistent with experience with helicopter inertial particle separators [9].

The axial velocity in the separator is limited by the ram pressure. If the air is discharged to ambient pressure without de-swirling and no other losses are counted, the condition $q_\infty \geq q_{\mathrm{ax}}\,(1 + \Delta p/q_{\mathrm{ax}})$ with the static-pressure drops of Table 9 gives $V_{\mathrm{ax}} \leq 0.91$, 0.81 and 0.69 times the flight speed for vane angles of 30°, 45° and 60°, that is 16.3, 14.6 and 12.4 m/s at the loiter speed of 18 m/s. The fuel-cell stack, the heat exchangers, and the outlet add further losses and reduce these limits, so that at loiter the cut size for sand at β = 45° increases to about 4.2 µm or more. The illustrative separator passes only $\pi R^2 V_{\mathrm{ax}} \approx 1.5$ m³/min at 20 m/s, whereas the cooling air requires 6.2–8.3 m³/min at cruise (Sect. 2.3). Two separators of about 57–66 mm diameter, one in each wing-root intake, would therefore be needed, and because the cut size grows in proportion to the radius at constant velocity and length, the swirl section would have to be lengthened accordingly. These results favour vane angles of 30–45° combined with a de-swirling stage over 60°, at which the static-pressure drop exceeds the axial dynamic pressure. The pressure loss of the complete intake will be measured in the wind tunnel.

7. Conclusions

A tri-source hybrid UAV for extreme climates has been presented, in which the PV array occupies the upper wing surface and a ram-air intake with a passive inertial separator and electrothermal anti-icing on the lower wing surface near the root supplies an open-cathode PEM fuel cell with both oxidant and cooling air. The main findings of the first-order assessment are:

- The sizing (MTOW 60 kg, S = 7.5 m², AR = 14, b = 10.25 m) is physically consistent: an independent low-fidelity analysis gives C_{D0} = 0.021–0.028, cruise and loiter power of 1.70–2.27 kW and 0.77–0.98 kW and hydrogen-only endurance of 5.3–7.1 h and 12.2–15.6 h, which bracket the design values.
- The intake air flow is dominated by the cooling requirement, about one to two orders of magnitude above the oxidant requirement, but two intakes with an effective diameter of about 6–7 cm each are sufficient; the separator pressure loss must stay well below the 160–310 Pa of available dynamic pressure.
- Under clear skies, the PV array covers about 30–45% of the 24-h loiter demand in the Libyan desert and up to 64% in the Arctic summer, but nothing in the polar night, which confirms the need for the hydrogen source and the common heating subsystem.
- A baseline internal arrangement that keeps the component positions of the patent application gives a centre of gravity at 29% of the mean aerodynamic chord, which moves by only 7 mm as the hydrogen is consumed; for a stable static margin, the wing had to be placed 1.55 m behind the nose, and the tail had to be enlarged to typical volume coefficients (V_H ≈ 0.41, V_V ≈ 0.020).
- The design C_{Lmax} of 1.4 requires a higher-lift airfoil than the NACA 4412.
- A three-dimensional RANS simulation of the clean configuration on three meshes gives a lift-curve slope of 5.63 per radian, a loiter angle of attack of about 2.0° and a neutral point 1.89 m behind the nose, which gives the baseline arrangement a static margin of about 13–14% of the mean aerodynamic chord; the computed drag is still mesh-dependent, so the component build-up remains the drag reference.
- Two-dimensional RANS simulations confirm the section lift data in the attached-flow range and show that the separator should use vane angles of 30–45° with a de-swirling stage; the PV installation must not trip the boundary layer near the leading edge of the wing, since a fully turbulent boundary layer would roughly double the profile drag at loiter.

Future work includes the wind-tunnel tests of Sect. 5, three-dimensional simulations of the intake and separator flow, a dynamic stability and control analysis, and cold-chamber testing of the fuel-cell pre-heating strategy.

Statements and declarations

Competing interests

The author is the inventor named in European patent application EP26211841.7, Tri-Source Hybrid Long-Endurance Unmanned Aerial Vehicle[13], which covers the configuration described in this paper.

Funding

No funding was received for conducting this study.

Data availability

The three-dimensional geometry model of Eastern Hornet is provided as Online Resource 1 (ZIP archive containing the model in glTF binary and OBJ formats at 1:1 scale in metres, an offline interactive viewer and a description file). The data underlying the figures and tables are available from the corresponding author upon reasonable request.

Code availability

The Python scripts, the Blender model script, the OpenFOAM case set-ups, and the mesh generators used for the sizing, the centre-of-gravity and sensitivity analyses, the aerodynamic assessment, the RANS simulations, the solar-yield calculation, and the figures are available from the corresponding author upon reasonable request. Development of the numerical scripts, model setups, and data post-processing tools utilized open-source analysis frameworks (including AeroSandbox, NeuralFoil, pvlib, OpenFOAM, Gmsh, and Blender) integrated within specialized computational workflows.

Appendix A: Protrusion drag estimates

The drag contribution of each protrusion was estimated as $\Delta C_{D0} = A\ C_D\ /\ S$, with A the frontal area and S the wing reference area. The low value corresponds to a faired or well-shaped item, and the high value to an unfaired one; typical coefficients were taken from [36]. All dimensions are those of the representative layout.

Table 12. Protrusion drag estimates

Item	Frontal area (m²)	C_D (low–high)	ΔC_{D0} (low–high)
Main wheels, 2 (0.40 × 0.17 m, tundra)	0.136	0.10–0.25	0.0018–0.0045
Nose wheel (0.34 × 0.12 m)	0.041	0.10–0.25	0.0005–0.0013
Leaf-spring legs (3, edge-on to the flow)	0.038	0.30–0.60	0.0015–0.0030
Gimbal sphere 1a (Ø 0.28 m)	0.062	0.25–0.40	0.0020–0.0032
Antennas, 1b/1c/1d fairings, other	0.030	0.25–0.50	0.0010–0.0020
Total			**0.0068–0.0140**

Added to the clean-airframe value of 0.0138, the total gives C_{D0} = 0.021–0.028.

References

1. Sornek, K., Augustyn-Nadzieja, J., Rosikoń, I., Łopusiewicz, R., Łopusiewicz, M.: Status and development prospects of solar-powered unmanned aerial vehicles—a literature review. Energies 18(8), 1924 (2025). https://doi.org/10.3390/en18081924.
2. Britton, N.: Airbus Zephyr crashes short of endurance record. AOPA News, 29 August 2022. https://aopa.org/news-and-media/all-news/2022/august/29/airbus-zephyr-crashes-short-of-endurance-record.
3. Felstead, P.: RIAT 2023: PHASA-35 completes first stratospheric flight trial. European Security & Defence, 19 July 2023. https://euro-sd.com/2023/07/news/32839/riat-2023-phasa-35-completes-first-stratospheric-flight-trial/.
4. Oettershagen, P., Melzer, A., Mantel, T., Rudin, K., Stastny, T., Wawrzacz, B., Hinzmann, T., Leutenegger, S., Alexis, K., Siegwart, R.: Design of small hand-launched solar-powered UAVs: from concept study to a multi-day world endurance record flight. J. Field Robot. 34(7), 1352–1377 (2017). https://doi.org/10.1002/rob.21717.
5. U.S. Naval Research Laboratory: NRL shatters endurance record for small electric UAV. NRL News, 9 May 2013. https://www.nrl.navy.mil/Media/News/Article/2563183/nrl-shatters-endurance-record-for-small-electric-uav/.
6. Mazur, A.M., Domanski, R.: Hybrid energy systems in unmanned aerial vehicles. Aircr. Eng. Aerosp. Technol. 91(5), 736–746 (2019). https://doi.org/10.1108/AEAT-08-2018-0218.

7. Engin, S., Çınar, H., Kandemir, İ.: A rule-based energy management technique considering altitude energy for a mini UAV with a hybrid power system consisting of battery and solar cell. Energies 17(16), 4056 (2024). https://doi.org/10.3390/en17164056.
8. Luo, Y., Jiao, K.: Cold start of proton exchange membrane fuel cell. Prog. Energy Combust. Sci. 64, 29–61 (2018). https://doi.org/10.1016/j.pecs.2017.10.003.
9. Filippone, A., Bojdo, N.: Turboshaft engine air particle separation. Prog. Aerosp. Sci. 46(5–6), 224–245 (2010). https://doi.org/10.1016/j.paerosci.2010.02.001.
10. Bojdo, N., Filippone, A.: A comparative study of helicopter engine air particle separation technologies. In: Proceedings of the 38th European Rotorcraft Forum (ERF 2012), Amsterdam, 4–7 September 2012, paper ERF2012_158. Netherlands Association of Aeronautical Engineers, Amsterdam (2012). http://hdl.handle.net/20.500.11881/646.
11. Wallace, F.: Hydrogen fuel cells power world's first solar-hydrogen-battery tribrid drone from H3 Dynamics and XSun. Hydrogen Fuel News, 16 June 2025. https://www.hydrogenfuelnews.com/hydrogen-fuel-cells-power-worlds-first-solar-hydrogen-battery-tribrid-drone-from-h3-dynamics-and-xsun/8571271.
12. Hüppauff, J., Pfaff, T., Blass, U., Motsch-Eichmann, N., Hausmann, J.: Integration of a novel hydrogen pressure vessel into small aircrafts. CEAS Aeronaut. J. 17, 611–626 (2026). https://doi.org/10.1007/s13272-025-00859-6.
13. Göker, Ü.D.: Tri-source hybrid long-endurance unmanned aerial vehicle. European patent application EP 26211841.7, filed October 2026.
14. Hexcel Corporation: HexPly 8552 epoxy matrix, product data sheet (EU version). https://hexcel.com/wp-content/uploads/2025/12/HexPly_8552_eu_DataSheet1.pdf. Accessed 26 October 2026.
15. 3M: 3M™ Polyurethane Protective Tape 8663HS, product page. https://www.3m.com/3M/en_US/p/d/b40069199/. Accessed 26 October 2026.
16. Unmanned Systems Technology: H3 Dynamics – Aerocell fuel cells, product page. https://www.unmannedsystemstechnology.com/company/h3-dynamics/aerocell-fuel-cells/. Accessed 26 October 2026.
17. Donateo, T.: Simulation approaches and validation issues for open-cathode fuel cell systems in manned and unmanned aerial vehicles. Energies 17(4), 900 (2024). https://doi.org/10.3390/en17040900.
18. Kim, R.-W., Hwang, K.-H., Kim, S.-R., Lee, J.-H.: Investigation of ultra-high pressure gas control system for hydrogen vehicles. Energies 13(10), 2446 (2020). https://doi.org/10.3390/en13102446.
19. ISO 19882:2018: Gaseous hydrogen — Thermally activated pressure relief devices for compressed hydrogen vehicle fuel containers. International Organization for Standardization, Geneva (2018).
20. Ball, M.: Leaf-sprung landing gear developed for heavy UAVs. Unmanned Systems Technology, 28 June 2019. https://www.unmannedsystemstechnology.com/2019/06/leaf-sprung-landing-gear-developed-for-heavy-uavs/.
21. Teledyne FLIR: Hadron 640R dual thermal/visible camera module, product specifications. https://www.flir.com/products/hadron-640r. Accessed 26 October 2026.
22. DJI Enterprise: Zenmuse H20N, product page. https://enterprise.dji.com/zenmuse-h20n. Accessed 26 October 2026.
23. DJI: Zenmuse L2, specifications. https://enterprise.dji.com/zenmuse-l2/specs. Accessed 8 November 2026.

24. DeltaQuad: AgEagle RedEdge-P and RedEdge-P Dual, payload specifications. https://www.deltaquad.com/payload/mapping/ageagle-rededge-p and https://www.deltaquad.com/payload/mapping/ageagle-rededge-p-dual. Accessed 8 November 2026.
25. Becker Avionics: BD406 Emergency Beacon Locator, Installation and Operation Manual DV16401.03, Issue 04. Becker Avionics GmbH, Rheinmünster (2021).
26. Starlink: Starlink Mini, specifications. https://www.starlink.com/specifications?spec=5. Accessed 8 November 2026.
27. Pratt, S.R., Raines, R.A., Fossa, C.E., Temple, M.A.: An operational and performance overview of the IRIDIUM low earth orbit satellite system. IEEE Commun. Surv. Tutor. 2(2), 2–10 (1999). https://doi.org/10.1109/COMST.1999.5340513.
28. ArduPilot Dev Team: The Cube Orange/+ with ADSB-In overview, ArduPilot documentation. https://ardupilot.org/plane/docs/common-thecubeorange-overview.html. Accessed 26 October 2026.
29. Raymer, D.P.: Aircraft Design: A Conceptual Approach, 6th edn. AIAA Education Series. American Institute of Aeronautics and Astronautics, Reston (2018).
30. Coles, D., Wadcock, A.J.: Flying-hot-wire study of flow past an NACA 4412 airfoil at maximum lift. AIAA J. 17(4), 321–329 (1979). https://doi.org/10.2514/3.61127.
31. Lemmon, E.W., Bell, I.H., Huber, M.L., McLinden, M.O.: Thermophysical properties of fluid systems. In: Linstrom, P.J., Mallard, W.G. (eds.) NIST Chemistry WebBook, NIST Standard Reference Database 69. National Institute of Standards and Technology, Gaithersburg. https://doi.org/10.18434/T4D303.
32. Ineichen, P., Perez, R.: A new airmass independent formulation for the Linke turbidity coefficient. Sol. Energy 73(3), 151–157 (2002). https://doi.org/10.1016/S0038-092X(02)00045-2.
33. Anderson, K.S., Hansen, C.W., Holmgren, W.F., Jensen, A.R., Mikofski, M.A., Driesse, A.: pvlib python: 2023 project update. J. Open Source Softw. 8(92), 5994 (2023). https://doi.org/10.21105/joss.05994.
34. Sharpe, P.D., Hansman, R.J.: AeroSandbox: a differentiable framework for aircraft design optimization. Report ICAT-2021-03, International Center for Air Transportation, Massachusetts Institute of Technology (2021). https://hdl.handle.net/1721.1/131194.
35. Sharpe, P., Hansman, R.J.: NeuralFoil: an airfoil aerodynamics analysis tool using physics-informed machine learning. arXiv:2503.16323 (2025). https://doi.org/10.48550/arXiv.2503.16323.
36. Hoerner, S.F.: Fluid-Dynamic Drag: Practical Information on Aerodynamic Drag and Hydrodynamic Resistance. Published by the author, Midland Park, N.J. (1965).
37. Weller, H.G., Tabor, G., Jasak, H., Fureby, C.: A tensorial approach to computational continuum mechanics using object-oriented techniques. Comput. Phys. 12(6), 620–631 (1998). https://doi.org/10.1063/1.168744.
38. Menter, F.R.: Two-equation eddy-viscosity turbulence models for engineering applications. AIAA J. 32(8), 1598–1605 (1994). https://doi.org/10.2514/3.12149.
39. Geuzaine, C., Remacle, J.-F.: Gmsh: a 3-D finite element mesh generator with built-in pre- and post-processing facilities. Int. J. Numer. Methods Eng. 79(11), 1309–1331 (2009). https://doi.org/10.1002/nme.2579.
40. Dixon, S.L., Hall, C.A.: Fluid Mechanics and Thermodynamics of Turbomachinery, 7th edn. Butterworth-Heinemann, Oxford (2014).

41. Roache, P.J.: Quantification of uncertainty in computational fluid dynamics. Annu. Rev. Fluid Mech. 29, 123–160 (1997). https://doi.org/10.1146/annurev.fluid.29.1.123.

Supplementary Files

This is a list of supplementary files associated with this preprint. Click to download.

- ESM1.zip